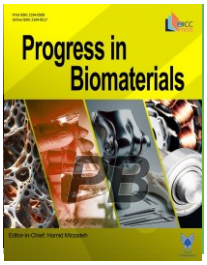

Volume 14, Issue 4, 2025: Article 1

Progress in Biomaterials (PIBM)

https://doi.org/10.57647/pibm.2025.1403.36

Graphene Oxide and Quantum Dot-Enhanced Alginate Scaffolds: Structural, Mechanical, and Biological Correlations for Neural Tissue Engineering Applications

Hanieh Shomali[1], Hamta Rahmatipour[1], Soheila Zamanlui Benisi[1*], Salar Mohammadi Shabestari[2] , Matin Mahmoudifard[3]

[1]*Department of biomedical engineering, CT.C., Islamic Azad University, Tehran, Iran*
[2]*Department of Polymer, School of Chemical Engineering, College of Engineering, University of Tehran, Tehran, Iran*
[3]*Department of Industrial and Environmental Biotechnology, National Institute for Genetic Engineering and Biotechnology (NIGEB), Tehran, Iran*

***Corresponding author:** s.zamanlui.te@gmail.com

Review Article:

Received:
9 August 2025

Accepted:
5 December 2025

Published in issue:
31 December 2025

Abstract

The integration of graphene-based nanomaterials into biopolymeric scaffolds offers a promising route to enhance mechanical, physicochemical, and biological performance for neural tissue engineering. In this work, alginate-based scaffolds incorporating graphene oxide (GO) and graphene quantum dots (GQDs) were fabricated via modified Hummer's and hydrothermal methods, respectively, at varying concentrations. Scanning electron microscopy (SEM) analysis revealed that GO increased surface roughness and formed interconnected porous networks, promoting superior cell adhesion and infiltration, while GQDs enhanced porosity but contributed less to mechanical reinforcement. Compressive strength improved significantly in GO-containing scaffolds (7 kPa) compared to GQDs (3 kPa), correlating with higher in vitro cell proliferation and adhesion. Attenuated total reflectance Fourier transform infrared spectroscopy (ATR-FTIR) confirmed nanomaterial integration into the alginate matrix. Swelling and degradation assays indicated faster degradation for AL-GQDs scaffolds, whereas conductivity testing showed higher electrical performance in GQDs-based scaffolds due to quantum confinement effects. Gene expression analysis revealed significant upregulation of PLCB1 and TRPV1 in AL-GO scaffolds, highlighting microarchitecture-mediated mechanotransduction. The presence of botulinum neurotoxin type A (BoNT/A) suppressed gene expression; however, AL-GO scaffolds maintained higher functional expression levels. Overall, scaffold and nanomaterial selection were shown to critically shape cellular responses, making AL-GO scaffolds promising candidates for neural tissue engineering.

Keyword: Graphene Oxide, Graphene Quantum Dots, Nanocomposite, Cell culture, porous scaffolds, Nerve cell

Cite this article: Shomali, H., Rahmatipour, H., Zamanlui Benisi, S., Mohammadi Shabestari, S. & Mahmoudifard, M., Graphene Oxide and Quantum Dot-Enhanced Alginate Scaffolds: Structural, Mechanical, and Biological Correlations for Neural Tissue Engineering Applications. Progress in Biomaterials 14(4), Article 1 (2025). https://doi.org/10.57647/pibm.2025.1403.36

Graphical abstract

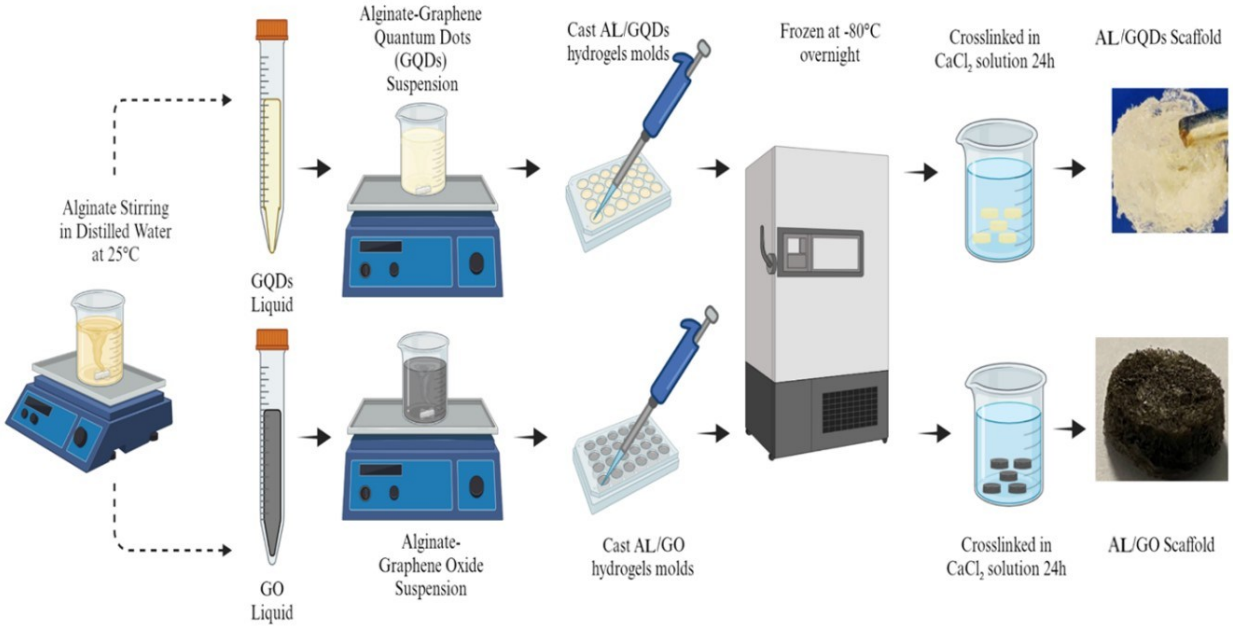

1. Introduction

Graphene-based nanomaterials, particularly graphene quantum dots (GQDs) and graphene oxide (GO), have emerged as highly promising candidates in the field of tissue engineering due to their unique structural and physicochemical characteristics. GQDs, typically smaller than 100 nanometers in size, exhibit remarkable electronic, optical, and biocompatible properties[1]. These quantum-scale materials, especially green GQDs synthesized through eco-friendly methods, represent an advanced class of carbon nanostructures with potential in regenerative medicine[2]. Similarly, GO, with its two-dimensional structure and high surface area, exists in various morphologies such as nanosheets, nanolayers, nanoplatelets, and nanoribbons[3]. Its surface functionality, mechanical robustness, and ability to form stable composites with polymers have positioned GO as a versatile component in scaffold fabrication[4]. Recent advances in nanomedicine have highlighted the biological effects of GQDs on stem cell behavior. For instance, Yang et al. [5] reported that GQDs at a concentration of 10 µg/mL significantly enhanced the proliferation of stem cells derived from human exfoliated deciduous teeth (SHED) and promoted osteogenic differentiation via the Wnt/β-catenin signaling cascade. In a parallel study, Geng et al. [6] demonstrated that negatively charged GQDs, in contrast to positively charged counterparts, effectively stimulated osteogenic differentiation through activation of the BMP/Smad signaling pathway. Incorporation of these GQDs into a gelatin methacryloyl (GelMA) matrix further improved bone regeneration outcomes in a calvarial defect model in mice. Beyond bone-related applications, GQDs have also shown significant promise in cardiovascular tissue repair. Si et al. [7] developed a conductive hydrogel incorporating ultra-small GQDs and human mesenchymal stem cells (hMSCs), which enhanced angiogenesis and reduced cardiomyocyte necrosis in myocardial infarction models. Likewise, Hou et al. [8] employed GO-derived and chemically modified GQDs to label human skin fibroblasts within scaffolds, enabling efficient long-term cell tracking without impairing cellular viability or function. GO has independently been recognized for its biofunctional interfaces and antibacterial properties, which are critical in orthopedic and tissue engineering contexts[9]. Prakash et al. [10] synthesized a GO-based composite via gel casting for application in orthopedic implants. Their study revealed notable antibacterial effects against both Gram-positive and Gram-negative bacterial strains, including *E. coli*, *S. mutans*, *S. aureus*, and *P. aeruginosa*. These findings underscore GO's potential for reducing implant-associated infections and enhancing scaffold bioactivity. Furthermore, bioinks containing GO-polymer composites have been utilized for fabricating vascularized bone constructs through three-dimensional bioprinting[11]. The functional groups present on the GO surface—including hydroxyl, epoxy, ketone, carboxyl, and diol moieties—facilitate strong interactions with biological molecules such as polysaccharides, proteins, aptamers, and nucleic acids[12]. This chemical versatility supports the integration of GO within polymeric matrices for enhanced mechanical and biological performance[13]. Studies have shown that incorporating GO into gelatin-

alginate scaffolds improves cell attachment, proliferation, and osteogenic differentiation. Purohit et al. [14] demonstrated that GO-based nanocomposites exhibit increased compressive strength, high hydrophilicity, and prolonged biodegradation, making them ideal for supporting tissue regeneration. Although numerous studies have investigated the individual applications of GO and GQDs in scaffold design, their combined effect within alginate (AL)-based systems remains insufficiently explored. Most prior research has focused either on enhancing mechanical integrity or improving biological performance independently, often overlooking the synergistic potential of co-functionalization with both nanomaterials. Additionally, only a limited number of studies have provided an integrated evaluation of scaffold behavior across structural, physicochemical, electrical, and cellular domains. This study was designed to address these gaps by systematically investigating the combined impact of GO and GQDs on the multifunctional performance of alginate-based scaffolds for tissue engineering. At the time of project initiation, the literature lacked a comprehensive comparison of scaffold behavior in terms of both bioactivity and mechanical enhancement through dual carbon nanomaterial incorporation. A comprehensive set of analyses—including transmission electron microscopy (TEM), scanning electron microscopy (SEM), and Fourier-transform infrared spectroscopy (FTIR)—was employed for material characterization. Key functional properties, including porosity, compressive strength, swelling behavior, degradation kinetics, electrical conductivity, cell viability, proliferation capacity, and gene expression profiles, were evaluated to assess scaffold performance and their potential applicability in regenerative medicine.

2. Materials and Methods

2.1. Chemicals and Reagents

The materials used in this study include Sodium Alginate (Merck), Calcium Chloride ($CaCl_2$) (Merck), Distilled Water, Dulbecco's Modified Eagle's Medium (DMEM), Fetal Bovine Serum (FBS), Trypsin, Phosphate Buffered Saline (PBS), Penicillin-Streptomycin (Gibco), Glutaraldehyde, Dimethyl Sulfoxide (DMSO) (Dnabiotech). Graphite meshes (size < 200 mm), ammonia solution (25%), dimethylformamide (DMF), sulfuric acid (95–97%), sodium nitrate ($NaNO_3$), oxygen peroxide (H_2O_2) (30%), sulfuric acid (H_2SO_4), potassium permanganate ($KMnO_4$), polytetrafluoroethylene (PTFE), ethanol, botulinum neurotoxin (BoNT), and HCl (97%) were purchased from Merck (Germany).The C6 Glioma Cell Line was used for evaluating scaffold biocompatibility, cell viability, and gene expression. This cell line is widely recognized for its relevance in modeling glioblastoma behavior. The equipment used in this research included a Microplate Reader for ELISA and MTT assays, a SEM for morphological analysis of scaffolds, a Freeze-Dryer for scaffold preparation, and an Ultrasonic Bath Sonicator for sample dispersion and nanoparticle preparation.

2.2. The synthesis procedure of nanomaterials

This section details the synthesis procedures for two nanomaterials: GO and GQDs

2.2.1. *Synthesis of GO*

GO was synthesized using a modified Hummer's method [15], previously optimized in our laboratory to improve oxidation efficiency and structural integrity. The process began by pre-cooling 46 mL of concentrated sulfuric acid (H_2SO_4, 95–97%) in an ice bath under continuous magnetic stirring at approximately 400 rpm. 1 gram of graphite powder was gradually added to the acid to ensure homogenous dispersion and to prevent local overheating. After 15 minutes of stirring, 1 g of sodium nitrate ($NaNO_3$) was introduced to promote intercalation between the graphite layers and facilitate the subsequent oxidation reaction. Following this step, 6 g of potassium permanganate ($KMnO_4$) was slowly added to the suspension while carefully maintaining the temperature below 20°C. This controlled addition minimized the risk of violent exothermic reactions and ensured uniform oxidation. The mixture was then stirred at approximately 40°C for 3 hours under continuous magnetic stirring, allowing for the gradual formation of manganese oxide intermediates and the development of a dark brown color, indicating successful oxidation of the graphite lattice. Subsequently, 80 mL of deionized water was added dropwise, causing a rise in temperature due to the exothermic nature of the dilution step. The temperature was stabilized at 80–85°C and maintained for 30 minutes to ensure complete oxidation. Upon cooling to room temperature, 200 mL of additional deionized water was added, followed by slow dropwise addition of 6 mL hydrogen peroxide (H_2O_2, 30% v/v). The reaction between residual $KMnO_4$ and H_2O_2 resulted in the evolution of oxygen and a distinct color change from dark brown to yellow, confirming the complete decomposition of excess permanganate and the formation of oxidized graphite species. The resulting dispersion was filtered and subjected to sequential washing purification procedure clarified. Initially, 10% (w/w) hydrochloric acid (HCl) was used to eliminate manganese residues and metal ions. Multiple washes with deionized water followed until the pH of the filtrate

reached approximately 6, ensuring removal of all acidic and ionic contaminants purification endpoint defined. The solid product, identified as graphite oxide, was collected on a cellulose-based filter membrane and dried under ambient conditions at temperatures not exceeding 38°C to preserve its layered structure. To produce exfoliated GO nanosheets, the dried graphite oxide was redispersed in deionized water at a concentration of 2 mg/mL and treated using an ultrasonic probe sonicator at 200 W, 20 kHz for 30 minutes. Ultrasonication disrupted the van der Waals forces between layers, yielding stable colloidal GO with high surface area and monolayer or few-layer architecture suitable for further functionalization. A schematic representation of the entire synthesis process is presented in Figure 1.

2.2.2. *Synthesis of GQDs*

GQDs were synthesized using a hydrothermal cutting method[16] in which GO previously obtained from the modified Hummer's process served as the carbonaceous precursor. A total of 270 mg of dried GO powder was dispersed in 10 mL of anhydrous dimethylformamide (DMF, ≥99.8% purity) to promote exfoliation and facilitate uniform solvothermal reaction conditions. The suspension was magnetically stirred for 20 minutes at approximately 400 rpm and subsequently subjected to probe ultrasonication (200 W, 20 kHz) for an additional 30 minutes to ensure homogenous dispersion at the nanoscale level. The resulting brownish-black colloidal suspension was carefully transferred into a 30 mL Teflon-lined stainless steel autoclave reactor (filling volume 40% of the total reactor capacity), which was hermetically sealed to maintain internal pressure during heating. The reactor was placed in a laboratory oven and maintained at 200°C for 5 hours (heating rate 5°C/min). Under these conditions, the solvothermal reaction initiated oxidative fragmentation and carbon-core reconstruction processes, leading to the formation of fluorescent carbon-based nanodots with well-defined size distributions. The appearance of a clear orange hue in the final product solution indicated the successful formation of GQDs with uniform particle size and optical characteristics. Following completion of the reaction, the autoclave was allowed to cool naturally to room temperature. The reaction mixture was then filtered using a 0.22 µm cellulose acetate membrane (vacuum-assisted filtration) to remove any unreacted residues or larger aggregates. The clarified filtrate was subjected to freeze-drying for 24 hours under reduced pressure to obtain solid GQDs powder. The dry product was stored at 4°C in a sealed, desiccated environment to maintain its photoluminescent stability and prevent agglomeration prior to subsequent use. A schematic diagram illustrating the synthesis steps of GQDs is provided in Figure 2 to facilitate process visualization.

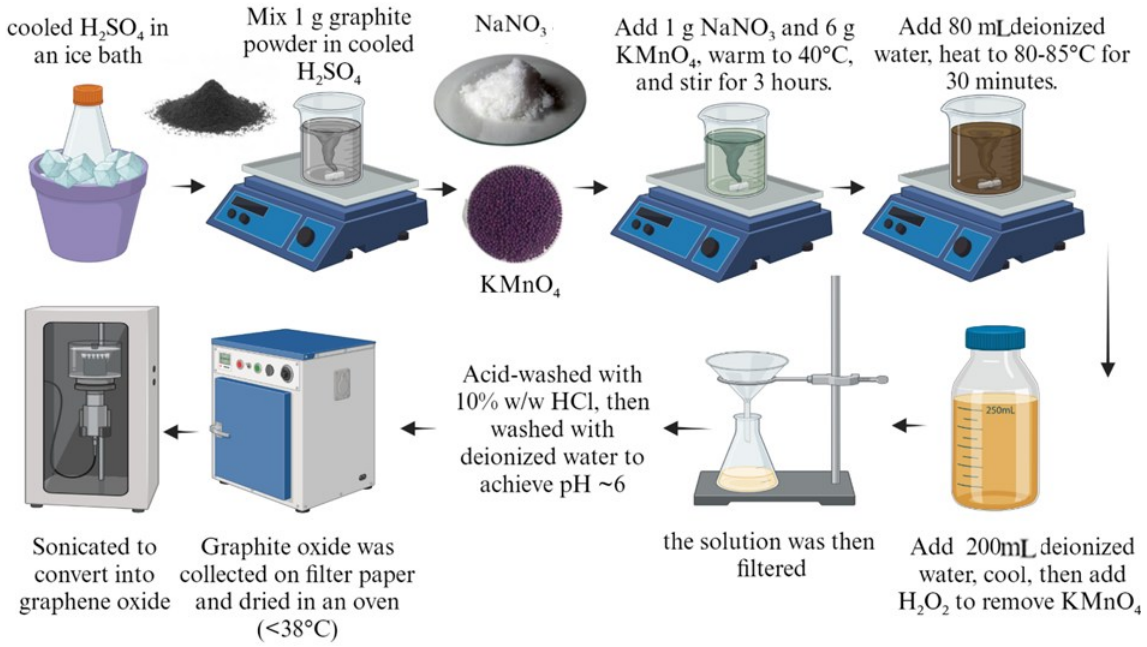

Figure 1. Synthesis of GO via a modified Hummer's method

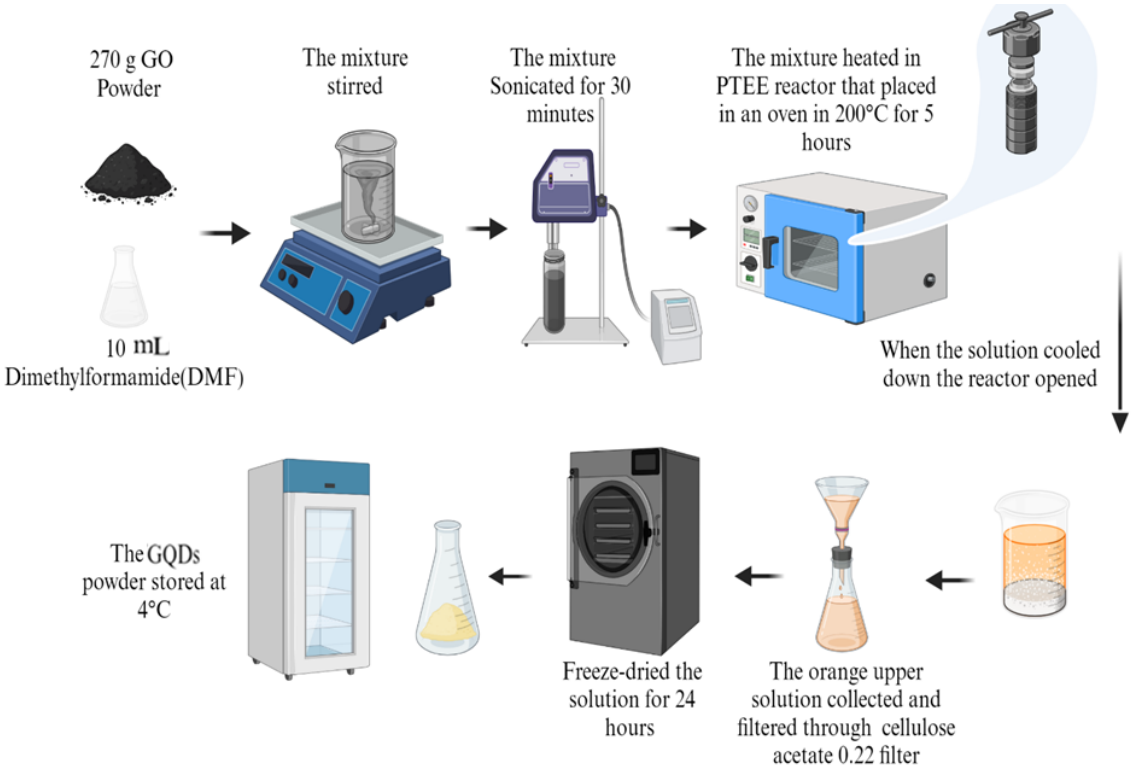

Figure 2. Synthesis of GQDs via a hydrothermal method

2.3. Preparation of the Hydrogel Scaffold

AL-based hydrogel scaffolds were fabricated through a multistep process designed to ensure uniform nanomaterial dispersion and reproducible three-dimensional structural integrity. Initially, medium-viscosity sodium alginate was dissolved in deionized water at a concentration of 2 wt% under continuous magnetic stirring at 500 rpm for 1 h at room temperature (25 ± 2°C) to obtain a homogeneous polymeric solution. This solution served as the primary hydrogel-forming matrix. In parallel, GO and GQDs were each dispersed separately in deionized water at concentrations of 0.5, 1.0, and 1.5 wt%. GO dispersions were subjected to probe ultrasonication at 200 W and 20 kHz for 60 min to promote nanosheet exfoliation and suppress agglomeration, while GQD dispersions were sonicated for 20 min under identical conditions to ensure colloidal stability and uniform particle distribution.

Following sonication, each nanoparticle suspension was added dropwise to the alginate solution under continuous magnetic stirring at 500 rpm and blended for an additional 60 min. This controlled mixing step facilitated homogeneous nanomaterial distribution within the alginate matrix and minimized interfacial aggregation, which is essential for maintaining the physicochemical and biological functionality of the scaffolds. To initiate ionic crosslinking and hydrogel formation, a 2 wt% aqueous solution of calcium chloride ($CaCl_2$) was added dropwise to the nanoparticle-containing alginate mixtures at a volume ratio of 1:1 between the alginate solution and $CaCl_2$ solution, while gently stirring with a sterile spatula for approximately 5 min. The divalent calcium ions induced ionic crosslinking between the guluronic acid blocks of alginate chains, resulting in cohesive and mechanically stable hydrogel networks incorporating GO or GQDs. The resulting hydrogels were subjected to a two-step structural stabilization process. First, samples were frozen at −80°C for 24 h to preserve the internal pore architecture and immobilize the hydrogel structure. Subsequently, the frozen scaffolds were freeze-dried at a condenser temperature of −50°C under vacuum below 0.1 mbar for 48 h to remove water via sublimation, yielding porous three-dimensional scaffolds suitable for tissue engineering applications. All scaffold formulations were prepared using at least three independently fabricated batches, and each experimental characterization was performed in triplicate to ensure reproducibility and statistical reliability.

2.4. Characterization

2.4.1. *Microscopic analyses and porosity evaluation*

For microscopic and structural characterization, scaffold samples were initially washed using a combination of

ethanol and deionized water in an ultrasonic bath (Elma, Germany) for 20 minutes to eliminate residual surface contaminants. For bulk samples, electrical conductivity was enhanced by affixing aluminum conductive adhesive tape to the specimen edges. To further improve surface conductivity and imaging resolution, samples were sputter-coated with a thin layer of conductive metal via the Physical Vapor Deposition (PVD) method using a COXEM instrument. High-resolution imaging was performed using a scanning electron microscope (SEM QUANTA 200, USA) equipped with both backscattered electron (BSE) and secondary electron (SE) detectors. Elemental composition was analyzed using an energy-dispersive X-ray spectroscopy (EDS) system with a silicon drift detector (EDAX, USA), enabling semi-quantitative analysis of carbon, oxygen, and other trace elements present in the nanostructured scaffolds. Scanning electron microscopy (SEM) and transmission electron microscopy (TEM) were employed as complementary techniques to evaluate the microstructural features of GONPs and GQDs. SEM was primarily utilized to assess the surface morphology and pore architecture of the composite scaffolds, with attention to uniformity, interconnected porosity, and dispersion of nanomaterials. TEM analysis was conducted to provide detailed insights into the nanoscale structure of the individual materials. For GONPs, characteristics such as sheet morphology, flake size, and thickness were examined, while for GQDs, particle size distribution, shape uniformity, and colloidal dispersion were evaluated with nanometer-level resolution. The integration of both techniques allowed for comprehensive structural profiling and correlation of micro- and nano-scale features.
Porosity was determined using a liquid displacement and uptake-based method according to the Archimedes principle. Briefly, dried scaffolds were immersed in ethanol, which was selected as the displacement fluid due to its low surface tension and minimal chemical interaction with polymeric matrices. A specific gravity bottle was employed for accurate volumetric measurements. The porosity value was calculated based on the mass changes before and after immersion using Equation (1). It should be noted that this approach reflects the apparent porosity, which accounts for the accessible pore volume and liquid uptake behavior of the scaffold. In highly hydrophilic and swellable alginate-based systems, ethanol can penetrate both the pore network and the polymer matrix, leading to apparent porosity values exceeding 100%. Therefore, the reported porosity values represent pore accessibility and absorption capacity rather than true volumetric porosity[17]:

$$\text{Porosity (\%)} = \frac{(W_2 - W_3 - W_s)/\rho_e}{(W_1 - W_3)/\rho_e} \quad (1)$$

where W_1 stands for the weight of the specific gravity bottle (0.03 M $CaCl_2$), W_2 shows the weight of the specific gravity bottle with $CaCl_2$ and scaffolds, W_3 demonstrates the weight of the specific gravity bottle considered after removing the W_2 scaffold, W_s the initial weight of scaffold, and finally, ρ_e stands for the density of the desired amount of $CaCl_2$ in the solution.

2.4.2. *Compressive strength and swelling evaluation*

The mechanical stability of the scaffolds was assessed by measuring their compressive strength using a universal testing machine (UTM). Cylindrical scaffold samples with uniform dimensions were subjected to uniaxial compression under a constant crosshead speed until complete structural failure occurred. The peak force recorded during deformation was considered the maximum load-bearing capacity, which was then used to calculate compressive strength. This mechanical parameter serves as a critical indicator of the scaffold's ability to maintain structural integrity under physiological loads, particularly in load-bearing tissue engineering applications.
To evaluate the swelling behavior, dried scaffolds were immersed in phosphate-buffered saline (PBS, pH 7.4) at room temperature. Scaffold diameters were recorded both before and after immersion at predefined time intervals to monitor dimensional changes due to fluid uptake. The swelling capacity reflects the scaffold's hydrophilic character and fluid retention capability, which are essential for nutrient diffusion, cell infiltration, and mechanical compliance in a biological environment. The swelling ratio was calculated using the equation (2)[18]:

$$S = \frac{D_{wet} - D_{dry}}{D_{dry}} \times 100 \quad (2)$$

D_{wet} and D_{dry} are the diameters of the swollen and dry scaffold, respectively.

2.4.3. *ATR-FTIR evolution*

The chemical composition and functional group distribution of the fabricated scaffolds were evaluated using attenuated total reflectance Fourier-transform infrared spectroscopy (ATR-FTIR) operated in reflective mode. This technique enables non-destructive surface analysis and is particularly suitable for biomaterial systems with complex organic-inorganic compositions. Spectral data were collected for each scaffold formulation and compared against reference spectra of the individual pure components to confirm the successful incorporation and retention of the constituent materials. The obtained spectra were interpreted to identify characteristic absorption peaks associated with specific functional groups, including hydroxyl, carboxyl, carbonyl, ether, and epoxide moieties, which are indicative of the presence of alginate, graphene oxide, and graphene quantum dots within the composite

structure. The spectral analysis covered a wavenumber range from 600 to 4000 cm^{-1}, encompassing both fingerprint and functional group regions. Key absorption bands were assigned based on established spectroscopic libraries, ensuring precise identification of chemical bonds and molecular interactions within the scaffold matrix. Variations in peak position and intensity among different scaffold formulations provided insight into potential chemical interactions, hydrogen bonding, and changes in polymer-nanoparticle compatibility.

2.4.4. *Cell culture and treatment*

The C6 glioma cell line was employed in this study due to its well-established relevance as a syngeneic model for glioblastoma research. Glioblastoma multiforme is characterized by rapid proliferation, aggressive invasiveness, and extensive vascularization, all of which are effectively mirrored by the C6 model in rat systems. Unlike xenograft-based models that require immunodeficient hosts, the use of C6 cells in immunocompetent rodents offers a biologically relevant tumor microenvironment with preserved immune interactions. Moreover, C6-derived gliomas exhibit several histological and morphological similarities to human glioblastoma, including the formation of dense peritumoral zones and modification of native vasculature, making them suitable for evaluating tumor–biomaterial interactions[19]. For *in vitro* assessment, C6 cells were cultured in Dulbecco's Modified Eagle Medium (DMEM) supplemented with 10 percent fetal bovine serum (FBS) and 1 percent penicillin-streptomycin. The cells were maintained under standard culture conditions at 37°C in a humidified incubator with 5 percent carbon dioxide. Prior to seeding, scaffolds were sterilized using UV irradiation and weighed precisely at 8 mg per sample. A seeding density of 1.5×10^5 cells per scaffold was selected to ensure uniform cellular distribution across the scaffold surface and internal pores. To evaluate the biological response to therapeutic modulation, selected scaffold groups were treated with 0.1 nanomolar concentrations of botulinum neurotoxin type A (BoNT/A). This treatment was designed to assess both the cytocompatibility of the scaffold matrices and their influence on cellular behavior under neuroactive stimulation. Biological evaluations, including cell viability and gene expression analysis, were performed at three time points: days 1, 3, and 7 following BoNT/A exposure.

2.4.5. *diphenyl-2H-tetrazolium bromide (MTT) assay*

To assess the cytocompatibility of the scaffolds, the MTT assay was conducted over a seven-day experimental period. Scaffolds were initially sterilized under ultraviolet light and transferred into individual wells of a 24-well culture plate containing 2 mL of complete culture medium. Following overnight equilibration, C6 glioma cells were seeded onto the scaffolds at a defined density. The experimental groups included pristine AL, alginate with graphene oxide (AL-GO), and alginate with graphene quantum dots (AL-GQDs), both with and without botulinum neurotoxin type A (BoNT/A) treatment.

Cell viability was evaluated at three time points: days 1, 3, and 7 post-seeding. At each time point, 150 microliters of MTT reagent (5 mg/mL in phosphate-buffered saline) were added directly to each well, and the plates were incubated for 4 hours at 37°C under standard culture conditions. During this period, metabolically active cells reduced the yellow tetrazolium salt to insoluble purple formazan crystals. Upon completion of incubation, the culture medium containing unreacted dye was removed, and the formazan crystals were solubilized in 150 microliters of dimethyl sulfoxide (DMSO) per well.

The absorbance of the resulting solution was measured at 570 nanometers using a microplate reader to quantify cell viability[20]. Each experimental condition was tested in quintuplicate to ensure statistical robustness. The viability percentage was calculated relative to the control group (untreated cells without scaffolds or BoNT/A exposure) using the equation (3)[18]:

$$\%\text{Viability} = \frac{OD_{test}}{OD_{control}} \times 100 \quad (3)$$

In this equation, OD_{test} represents the optical density (OD) of the wells containing the treated scaffold samples, while $OD_{control}$ represents the optical density of the wells containing untreated cells cultured under the same conditions without scaffold or BoNT/A (control group).

2.5. Gene expression analysis

Gene expression analysis was conducted to evaluate the impact of scaffold composition and BoNT/A treatment on cellular signaling pathways. The study aimed to determine whether the incorporation of GO or GQDs into alginate-based scaffolds could modulate gene expression patterns in C6 glioma cells and whether this modulation was influenced by neuroactive stimulation. Comparative assessments were performed across experimental groups including AL-GO and AL-GQDs scaffolds, both with and without BoNT/A exposure, to identify scaffold-dependent transcriptional responses. Quantitative real-time polymerase chain reaction (qPCR) was employed to quantify mRNA expression levels of target genes. This technique offers two principal modes of analysis: absolute quantification, which involves constructing a standard curve to determine exact transcript numbers, and relative quantification, which compares gene expression levels in treated samples to those in a defined reference group. In this study, the relative quantification method was selected

due to its procedural simplicity, cost-effectiveness, and ability to minimize variability associated with standard curve generation. The relative approach also allows for direct comparison of transcriptional changes among treatment conditions, thereby providing more functionally meaningful insights into scaffold-induced cellular responses. All gene expression levels were normalized against an internal housekeeping gene, and fold changes were calculated using the $2^{-\Delta\Delta Ct}$ method to determine statistically significant differences in expression across the experimental conditions.

2.5.1. *Reverse transcription-polymerase chain reaction (RT-PCR)*

Total RNA was extracted from cell-seeded scaffold samples using the RNX-Plus reagent (Sina Clone, Tehran, Iran) in accordance with the manufacturer's protocol. The purity and concentration of the extracted RNA were verified by spectrophotometric analysis, and the RNA was immediately reverse-transcribed into complementary DNA (cDNA) using the Vira Gene reverse transcription kit to ensure high-fidelity synthesis suitable for quantitative gene expression analysis. Quantitative real-time polymerase chain reaction (qPCR) was performed using a SensoQuest Biomedizinische thermal cycler. SYBR Green PCR Master Mix was employed as the fluorescent intercalating dye to monitor DNA amplification in real time. The qPCR reactions were prepared using gene-specific primers targeting the following genes:

- **TRPV1**: Forward 5′-CATCTTCACCACGGCTGCTTAC-3′, Reverse 5′-CAGACAGGATCTCTCCAGTGAC-3′
- **PLCB1**: Forward 5′-GCCCCTGGAGATTCTGGAGT-3′, Reverse 5′-GGGAGACTTGAGGTTCACCTTT-3′
- **GAPDH (internal control)**: Forward 5′-CATTGCTGACAGGATGCAGAAGG-3′, Reverse 5′-TGCTGGAAGGTGGACAGTGAGG-3′

Thermal cycling conditions consisted of an initial denaturation step at 95°C for 18 seconds, followed by 40 amplification cycles comprising denaturation at 95°C for 18 seconds, annealing at 58°C for 60 seconds, and extension at 55°C for 60 seconds. All reactions were performed in triplicate to ensure reproducibility. The selection of PLCB1 (Phospholipase C Beta 1) and TRPV1 (Transient Receptor Potential Vanilloid 1) as target genes was based on their critical roles in neural signaling pathways. PLCB1 is a pivotal enzyme within the phosphoinositide signaling cascade, responsible for the hydrolysis of phosphatidylinositol 4,5-bisphosphate (PIP2) into the secondary messenger's inositol trisphosphate (IP3) and diacylglycerol (DAG). This pathway governs calcium ion mobilization, cell proliferation, and neural differentiation, thereby serving as a valuable marker for scaffold-induced modulation of intracellular signaling. In contrast, TRPV1 encodes a non-selective cation channel predominantly expressed in sensory neurons. It is activated by various stimuli such as heat, acidic pH, and capsaicin, and it plays a key role in calcium-mediated responses related to inflammation, nociception, and tissue regeneration. Monitoring TRPV1 expression provides insights into the scaffold's effects on neurofunctional plasticity and its potential role in promoting neural repair. By evaluating both PLCB1 and TRPV1 expression levels, this study aimed to capture a comprehensive view of scaffold–cell interactions, encompassing intracellular signaling dynamics and functional neuroregeneration under the modulatory influence of BoNT/A. Relative quantification of gene expression was performed using the $2^{-\Delta\Delta Ct}$ method, with GAPDH serving as the internal housekeeping gene. This approach enabled accurate assessment of expression fold changes across experimental conditions relative to the untreated control group.

2.6. Statistical analisis

All quantitative data are presented as mean ± standard deviation (SD) unless otherwise stated. All experiments were performed in triplicate (n = 3) using independently prepared samples. Statistical significance among multiple groups was assessed using one-way analysis of variance (ANOVA), followed by Tukey's post hoc test for pairwise comparisons. A p-value < 0.05 was considered statistically significant.

3.Results and discussion

3.1. SEM and TEM Characterization of synthesized nanoparticles

Figure 3 presents the morphological and structural features of synthesized GO and GQDs using SEM and TEM analyses. The SEM image of GO (Figure 3a) reveals a typical wrinkled and layered morphology, indicative of a sheet-like structure with partially exfoliated flakes. These features suggest the presence of few-layer GO with a high specific surface area, which is essential for enhanced physicochemical interaction in hydrogel matrices[21]. In contrast, the SEM image of GQDs (Figure 3b) shows a homogeneous distribution of small, spherical particles dispersed over a rough surface, consistent with the formation of nano-sized graphene derivatives[22]. TEM imaging was further employed to examine the internal morphology. The GO sample (Figure 3c) exhibits ultra-thin, transparent layers with slight folding and overlapping,

confirming its multi-layered nature and large lateral dimensions in the range of hundreds of nanometers. These sheet-like domains are essential for forming mechanically robust scaffolds and establishing electrostatic interactions with charged biomolecules[23]. More notably, the TEM image of GQDs (Figure 3d) confirms the successful formation of monodisperse, zero-dimensional quantum dots. The particles are uniformly distributed, exhibiting a quasi-spherical morphology[24]. Quantitative analysis revealed that the average particle diameter of GQDs was approximately 0.65 ± 0.09 nm, aligning with the expected size range of ultra-small GQDs produced via hydrothermal methods. The narrow size distribution underscores the efficacy of the synthesis protocol and highlights the potential of these nanomaterials for biomedical applications where precise dimensional control is critical for cellular uptake and bioactivity[25]. Overall, the SEM and TEM analyses confirm the successful synthesis of structurally distinct GO nanosheets and GQDs with desirable morphology and nanometric features, supporting their integration into alginate-based scaffolds for tissue engineering.

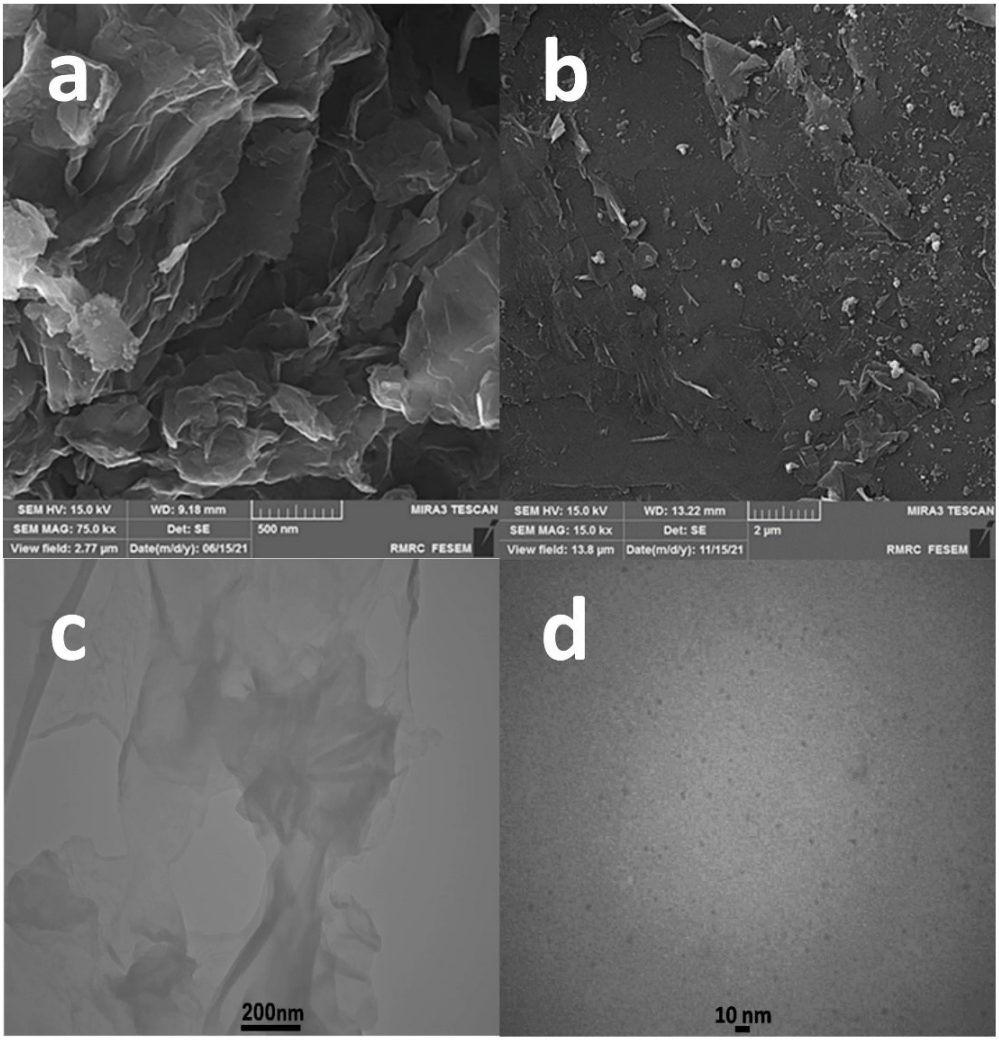

Figure 3. SEM images of a: GO, b: GQDs, and TEM images of c: GO and d: GQDs

3.2. AT-FTIR Characterization of AL, GO, and scaffolds

Figure 4 illustrates the ATR-FTIR spectra of AL, GO, GQDs, and the corresponding nanocomposite scaffolds (AL-GO and AL-GQDs), recorded in the range of 300 to 4300 cm^{-1}. The spectrum of pure AL exhibited characteristic absorption bands at approximately 3444 cm^{-1}, attributed to O–H stretching vibrations of hydroxyl groups, and at 2923 cm^{-1} corresponding to aliphatic C–H stretching vibrations [26]. Additional bands observed at 1619 and 1415 cm^{-1} were assigned to the asymmetric and symmetric stretching vibrations of carboxylate (COO^-) groups, respectively [27], while the band at 1029 cm^{-1} was associated with C–O stretching vibrations originating from ether linkages or pyranose ring structures [28]. These spectral features are consistent with the polysaccharide backbone of AL, which contains abundant hydroxyl and carboxyl functional groups capable of forming hydrogen bonding and ionic interactions [29]. The FTIR spectrum of GO displayed a broad O–H stretching band around 3444 cm^{-1}, reflecting the presence of hydroxyl groups and adsorbed water on the oxidized graphene surface. Distinct bands at 1619 cm^{-1}, associated with sp^2 carbon domains, and at 1415 cm^{-1}, related to oxygen-containing functional groups, were also observed. The presence of a band near 1029 cm^{-1} further confirmed C–O stretching vibrations associated with epoxide and alkoxy groups introduced during oxidation[30]. In the GQDs spectrum, a broad O–H stretching band centered around 3444 cm^{-1} was similarly observed, indicating surface hydroxyl functionalities. Bands located at 1619 and 1415 cm^{-1} were attributed to carboxylate groups and aromatic carbon domains, while the band at 1029 cm^{-1} was assigned to C–O stretching vibrations[31]. The presence and preservation of these characteristic bands reflect the functionalized surface chemistry of GQDs, which facilitates their dispersion and interaction within polymeric matrices. The AL-GO composite spectrum retained the characteristic bands of both alginate and GO, while notable band broadening and slight positional variationswere observed in the O–H and carboxylate regions. Such spectral changes indicate the formation of intermolecular interactions, primarily hydrogen bonding and electrostatic interactions, between alginate chains and oxygen-containing functional groups on GO[32]. The persistence of the C–O stretching band at approximately 1029 cm^{-1} further supports the molecular-level integration of GO within the alginate network. Similarly, the AL-GQDs spectrum exhibited broadened and slightly shifted bands in the O–H and carboxylate regions, suggesting strong intermolecular interactions between alginate and the surface functional groups of GQDs[33]. The retention of the characteristic C–O stretching band at 1029 cm^{-1} confirms the successful incorporation of GQDs into the alginate matrix without disruption of their surface chemistry. Overall, the observed band positions, shifts, and broadening across the composite spectra provide clear evidence of effective incorporation of GO and GQDs into the alginate hydrogel. These spectral features indicate the presence of hydrogen bonding and electrostatic interactions at the molecular level, which are known to influence the structural stability, hydration behavior, and biofunctional performance of polymer-based composite scaffolds.

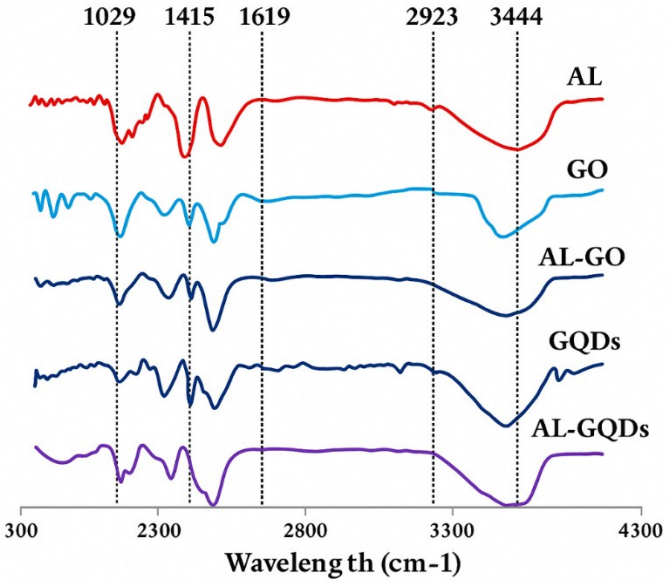

Figure 4. AT-FTIR spectra of AL, GO, AL-GO scaffold, GQDs, and AL-GQDs scaffold

3.3. Porosity and SEM of scaffolds

Figure 6 presents a comprehensive evaluation of the porosity and morphological characteristics of alginate-based scaffolds reinforced with GO and GQDs. The upper panel (Figure 5A) illustrates the porosity rate (%) of scaffolds containing different concentrations of nanomaterials (0%, 0.5%, 1%, and 1.5% w/w), while Figures 5B and 5C provide representative SEM images of the internal microstructure of AL-GO and AL-GQDs scaffolds at 0.5%, 1%, and 1.5% concentrations. Quantitative porosity analysis (Figure 5A) revealed that the incorporation of nanomaterials significantly influences the scaffold's porosity in a concentration- and structure-dependent manner. Pristine AL scaffolds exhibited an average porosity rate of approximately 112%, which remained statistically unchanged upon the addition of either GO or GQDs at 0% nanomaterial ($p > 0.05$). However, at 0.5% and 1% concentrations, AL-GQDs scaffolds demonstrated a significant increase in porosity compared to their AL-GO counterparts ($p < 0.001$). Specifically, AL-GQDs scaffolds reached porosity rates of approximately 142% and 148% at 0.5% and 1%, respectively, while AL-GO scaffolds exhibited a more modest increase to 115% and 118%. This disparity is primarily attributed to the morphological differences between GO and GQDs. GQDs, due to their zero-dimensional spherical structure and small size, tend to occupy interstitial voids without significantly restricting pore formation[34]. Their uniform dispersion at lower concentrations promotes a looser network architecture, resulting in enhanced porosity[35]. In contrast, GO nanosheets, with their two-dimensional lamellar structure, interact strongly with the AL matrix through hydrogen bonding and electrostatic interactions, which leads to a partial densification of the polymer network and consequently a moderate porosity increase[36]. At higher concentrations (1.5%), a reduction in porosity was observed in both AL-GO and AL-GQDs scaffolds compared to their 1% counterparts, though the decline was more pronounced in AL-GO. This reduction is likely due to nanoparticle agglomeration and network densification, which compromise pore connectivity and size[37]. In AL-GQDs scaffolds, despite the decrease, the porosity remained significantly higher than AL-GO, indicating better pore retention capacity due to the limited network crosslinking ability of GQDs. The morphological observations from SEM micrographs (Figures 5B and 5C) corroborate the quantitative porosity data. The AL-GO scaffolds exhibit a relatively compact and dense microstructure with smaller, well-distributed pores, which becomes increasingly compact at higher GO concentrations. This morphology is consistent with the hypothesis that GO sheets act as physical crosslinkers within the AL matrix, restricting excessive network expansion[38]. Conversely, the AL-GQDs scaffolds displayed a more open and interconnected pore architecture with larger pore diameters, particularly at 0.5% and 1%, supporting their higher porosity values. However, at 1.5% GQDs, signs of local aggregation and irregular pore distribution are evident, which aligns with the observed reduction in porosity at this concentration. The macroscopic images of AL-GO and AL-GQDs scaffolds further emphasize these structural differences. AL-GO scaffolds present a rigid, well-shaped architecture, indicative of enhanced mechanical stability, while AL-GQDs scaffolds appear softer and more gelatinous, reflecting their higher porosity and lower crosslinking density. Overall, these findings highlight the tunable nature of scaffold porosity through strategic selection and concentration adjustment of graphene-based nanomaterials. GO provides superior mechanical reinforcement with moderate porosity enhancement, whereas GQDs contribute to higher porosity with limited mechanical stiffening. Such tunability is essential for tailoring scaffolds for specific tissue engineering applications, where balancing porosity and mechanical integrity is crucial for optimizing cell infiltration, nutrient diffusion, and overall scaffold performance.

3.4. Compressive strength

The compressive strength of scaffolds plays a crucial role in determining their structural stability and mechanical compatibility for tissue engineering applications, particularly in load-bearing tissues such as bone and cartilage. Figure 6 illustrates the compressive modulus of AL-based hydrogels reinforced with either GO or GQDs at varying concentrations (0.5%, 1.0%, and 1.5% by weight), compared to the neat AL scaffold (0%). The results indicate a clear and progressive increase in compressive strength with increasing nanomaterial concentration in both AL-GO and AL-GQDs groups. The most significant enhancement was observed in AL-GO scaffolds containing 1.5 wt% GO, reaching a modulus of approximately 7 kPa, which represents a 55% increase compared to the neat AL control and 20% higher than the 0.5% GO scaffold. In comparison, AL-GQDs scaffolds with 1.5 wt% GQDs exhibited a peak modulus of 3 kPa, reflecting a ~30% increase over the control and 15% higher than the 0.5% GQDs scaffold. These differences were statistically significant ($p < 0.05$), as indicated in the figure. The superior mechanical performance of AL-GO scaffolds is primarily attributed to the inherent two-dimensional (2D) structure of GO nanosheets, which offer a high aspect ratio, extensive surface area, and abundant oxygen-containing functional groups (e.g., hydroxyl, carboxyl, epoxy)[39].

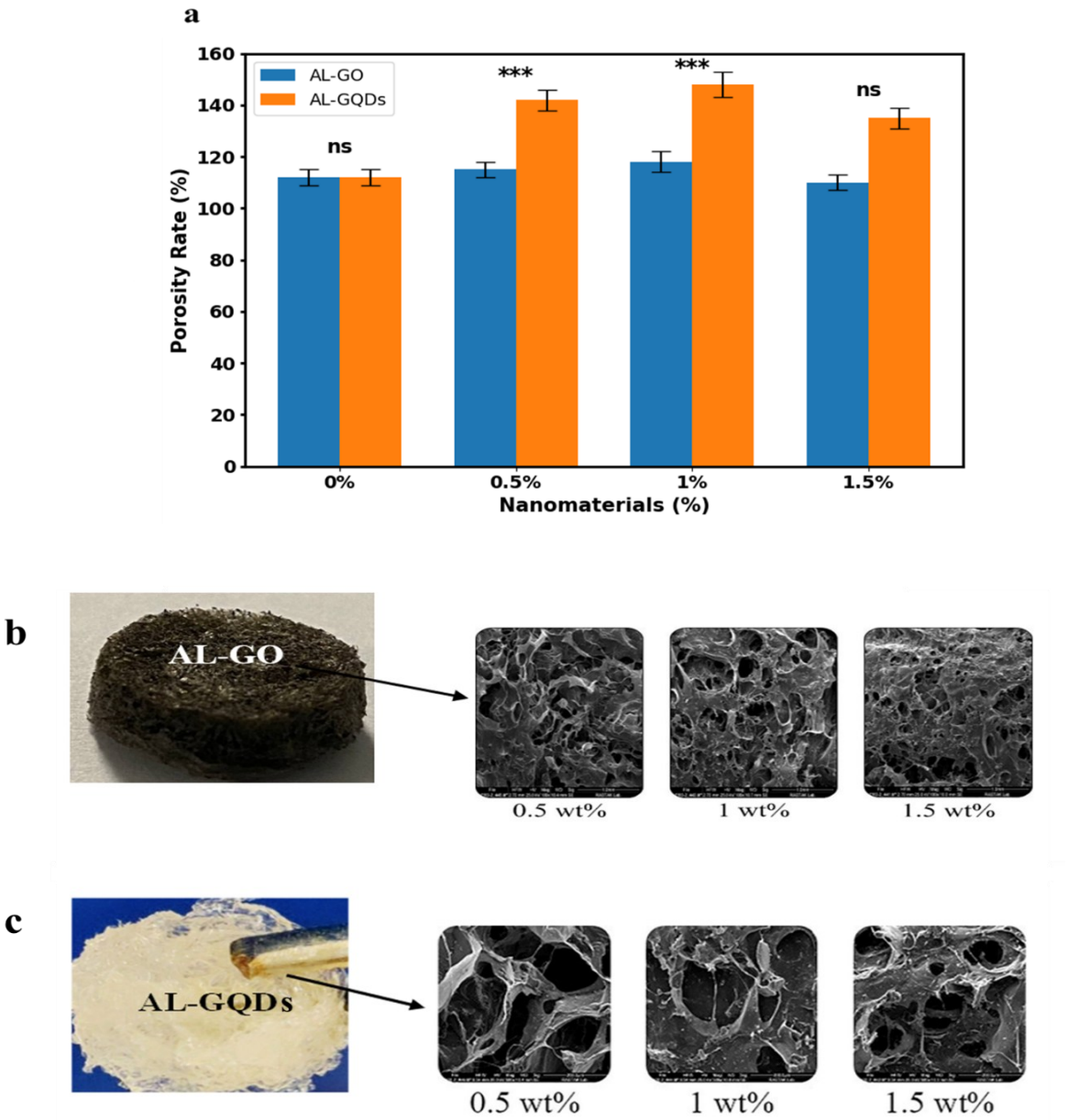

Figure 5. a: Porosity rate of AL, AL-GO and AL-GQDs scaffolds. Data are presented as mean ± SD from three independent experiments (n = 3). Statistical significance was evaluated using one-way ANOVA. *p < 0.05, ***p < 0.001; ns indicates no significant difference, b) and C: SEM images of composite scaffolds. (magnification is 100x and scale bars are 1mm), and AL and AL-GQDs scaffolds with SEM images

These features enable robust interfacial interactions with the polymeric matrix via hydrogen bonding, electrostatic forces, and van der Waals interactions, which collectively enhance load transfer efficiency within the scaffold[40]. Furthermore, the layered morphology of GO contributes to stress dissipation and energy absorption, resulting in improved mechanical resilience[41]. In contrast, GQDs possess a zero-dimensional (0D) spherical morphology with a much smaller size and lower surface-to-volume ratio. Although their surface contains functional groups that can engage in interactions with the AL matrix, the spatial confinement and lack of planar domains limit their capacity to form percolated reinforcing networks[42]. As a result, the enhancement in mechanical strength in AL-GQDs scaffolds is relatively modest and does not match the level achieved with GO. Additionally, the role of GO in increasing crosslinking density with calcium ions (Ca^{2+}) during ionic gelation should not be overlooked. The negatively charged functional groups on GO may facilitate ionic bridging with Ca^{2+}, thereby increasing network connectivity and stiffness. This effect is less pronounced in GQDs due to their limited interaction sites and smaller

interface with the surrounding matrix[43]. It is also important to consider the potential plateau or saturation behavior observed in AL-GQDs at 1.5 wt%. While a higher concentration generally leads to increased reinforcement, excessive nanoparticle loading may lead to agglomeration or phase separation, disrupting the homogeneity of the matrix and impeding uniform stress distribution[44]. This effect is well-documented in nanocomposite literature, where beyond a certain threshold, nanofillers may compromise rather than improve mechanical performance due to poor dispersion or interfacial debonding. These findings are consistent with previous reports that have emphasized the superior mechanical reinforcement potential of GO compared to other graphene derivatives, including GQDs, carbon dots, and reduced GO. The ability of GO to form a continuous and mechanically active network within polymer matrices renders it particularly suitable for developing hydrogels aimed at supporting structural integrity under physiological loads[45].

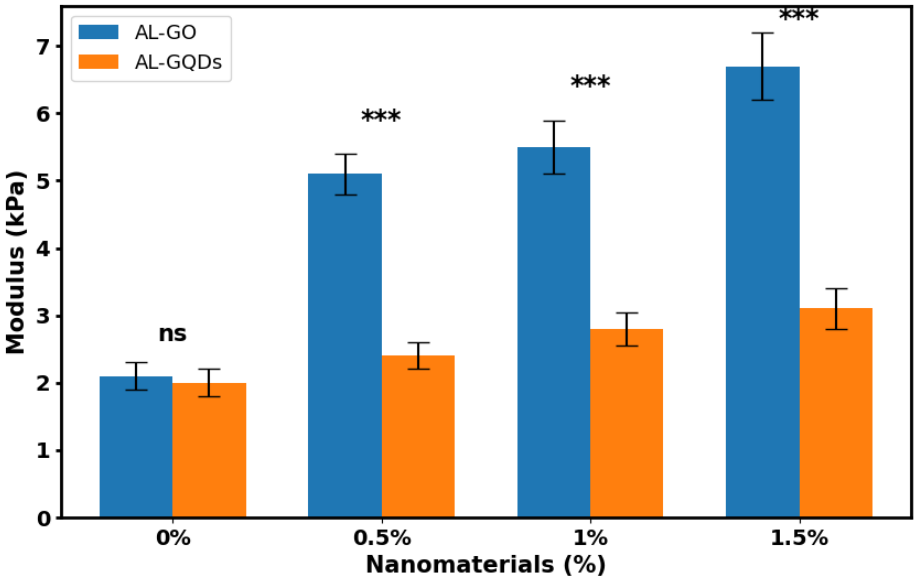

Figure 6. Compressive modulus of alginate-based hydrogels incorporated with different concentrations (0%, 0.5%, 1%, and 1.5% w/w) of GO and GQDs. A significant concentration-dependent enhancement in mechanical stiffness was observed for AL-GO scaffolds compared to AL-GQDs. Statistical significance between corresponding concentrations is indicated as follows: ns (not significant), *p < 0.05, **p < 0.01, ***p < 0.001 (n=3).

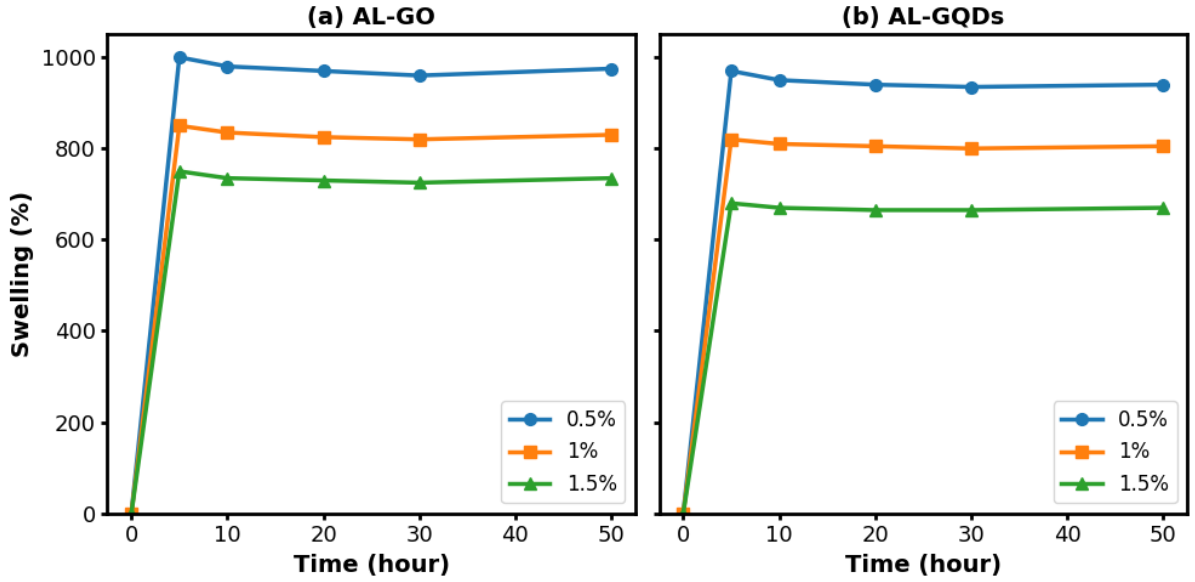

Figure 7. Swelling percentage of a) AL-GO scaffolds and b) AL-GQDs scaffolds

10.57647/pibm.2025.1403.36

3.5. Swelling degree

The swelling capacity of scaffolds is a critical parameter in tissue engineering, as it directly influences nutrient diffusion, cell infiltration, and overall scaffold functionality in a physiological environment. Figure 7 illustrates the swelling behavior of alginate-based hydrogels reinforced with GO and GQDs at concentrations of 0.5%, 1.0%, and 1.5% (w/w) over a 50-hour immersion period. For both AL-GO and AL-GQDs scaffolds, a rapid initial swelling phase was observed within the first 5 hours, reaching over 80% of their maximum swelling capacity. This immediate uptake can be attributed to the hydrophilic nature of sodium alginate and the porous architecture of the freeze-dried scaffolds, which facilitate rapid water absorption. Following this initial phase, a plateau was reached, indicating the equilibrium swelling state[46]. Notably, scaffolds reinforced with GO exhibited a higher equilibrium swelling ratio compared to those containing GQDs. At 0.5% GO, the swelling percentage stabilized around 980–1000%, whereas AL-GQDs at the same concentration reached approximately 950–970%. This difference, although subtle, suggests that the planar, sheet-like morphology of GO introduces additional microvoids and capillary channels within the hydrogel network, enhancing water retention capacity[47]. In contrast, the spherical morphology of GQDs, despite their nanoscale size, contributes less effectively to network expansion and pore interconnectivity[48]. As the concentration of nanomaterials increased to 1.0% and 1.5%, a concentration-dependent decrease in swelling capacity was observed in both systems. For AL-GO scaffolds, swelling decreased to approximately 850% at 1% and further to 740% at 1.5%. Similarly, AL-GQDs scaffolds exhibited a reduction to 810% at 1% and 670% at 1.5%. This inverse relationship between nanofiller content and swelling ratio is attributed to the densification of the hydrogel network due to the physical presence of nanomaterials and their interaction with alginate chains[49]. Specifically, GO nanosheets are known to form hydrogen bonds and electrostatic interactions with carboxyl and hydroxyl groups in AL, leading to a more compact and mechanically reinforced matrix, which restricts excessive water uptake[50]. This crosslinking effect is also present in GQDs-containing scaffolds but to a lesser extent, given the limited surface area and interaction domains of the zero-dimensional GQDs[51]. Another critical observation is the more pronounced decline in swelling capacity in AL-GQDs scaffolds at higher concentrations compared to AL-GO scaffolds. This can be explained by the tendency of GQDs to agglomerate at elevated loadings, which disrupts the homogeneity of the polymeric network and creates localized dense regions, thereby impeding uniform water diffusion[52]. In contrast, the extended planar structure of GO facilitates better dispersion and formation of continuous water-absorption pathways even at higher loadings[53]. These results suggest that while both GO and GQDs can modulate the swelling behavior of alginate-based hydrogels, the morphological characteristics and interfacial interaction capacity of GO enable a more controlled and tunable swelling response. This property is particularly advantageous for applications where scaffold hydration needs to be balanced with mechanical stability, such as in wound healing or cartilage regeneration[46]. In summary, the incorporation of GO leads to a higher and more stable swelling capacity due to its unique two-dimensional structure and strong matrix interaction, whereas GQDs exhibit a more limited reinforcement effect on the swelling behavior, especially at higher concentrations where aggregation effects become dominant. These findings are in agreement with previous reports highlighting the superior structural influence of GO in polymeric hydrogels compared to zero-dimensional graphene derivatives.

3.6. Biodegradatin

Figure 9 illustrates the in vitro degradation profiles of alginate-based scaffolds reinforced with varying concentrations of GO and GQDs over a 24-day period. Panels (a) and (b) represent the degradation behavior of AL-GO and AL-GQDs scaffolds, respectively, compared to pure alginate controls (No $NANO_3$). In AL-GO scaffolds (Figure 8a), a gradual and controlled degradation trend is observed across all concentrations. Initially, all groups exhibited minimal mass loss within the first 7 days, with degradation percentages ranging from 5% to 20%. After day 7, the degradation rate accelerated, reaching approximately 60%–65% by day 24. Notably, scaffolds containing higher GO concentrations (1% and 1.5%) demonstrated slightly reduced degradation rates compared to the 0.5% GO and pure AL control groups. This trend can be attributed to the structural reinforcement provided by GO nanosheets, which interact with the AL matrix through hydrogen bonding and electrostatic interactions, forming a denser and more stable network that resists enzymatic and hydrolytic breakdown. The planar morphology of GO further contributes to this stabilization by acting as a physical barrier against water penetration and polymer chain mobility[53]. Conversely, AL-GQDs scaffolds (Figure 8b) exhibited a markedly different degradation behavior. A steep initial degradation phase was observed, with mass loss exceeding 30% within the first 3 days. This rapid degradation can be attributed to the lower crosslinking density and weaker physical reinforcement imparted by GQDs, whose zero-dimensional structure and limited surface functionalization result in reduced

interfacial interactions with the AL matrix[54]. Although the degradation rate of AL-GQDs scaffolds decelerated beyond day 7, the total mass loss reached 90%–95% by day 24, significantly higher than the AL-GO counterparts. The presence of GQDs appears to promote localized matrix disruption and water uptake, thereby accelerating scaffold disintegration. A concentration-dependent effect was also observed in AL-GQDs scaffolds, with higher GQDs content (1% and 1.5%) marginally reducing the degradation rate compared to the 0.5% group. This slight retardation may be due to the increased probability of GQDs aggregation at higher loadings, which can create localized dense regions that offer some resistance to degradation[55]. However, this reinforcement is not comparable to the network-integrating capacity of GO sheets. These findings emphasize the critical influence of nanomaterial morphology and interaction mechanisms on the degradation kinetics of composite scaffolds. While GO facilitates structural stability and controlled degradation through its two-dimensional layered architecture and strong polymer interactions, GQDs, due to their nanoscale dimensions and limited binding affinity, induce a more rapid scaffold breakdown[56]. This differential degradation behavior can be strategically leveraged depending on the intended tissue engineering application. AL-GO scaffolds are better suited for long-term structural support in load-bearing tissues, whereas AL-GQDs scaffolds, with their faster degradation profile, may be advantageous for applications requiring rapid scaffold resorption and matrix remodeling, such as soft tissue regeneration. In summary, the degradation profiles presented in Figure 8 validate the tunability of scaffold resorption rates through selective incorporation of graphene-based nanomaterials, with GO offering sustained structural integrity and GQDs promoting accelerated biodegradability.

3.7. Electrical conductivity

Figure 8c illustrates the electrical conductivity of alginate-based scaffolds reinforced with GO and GQDs at concentrations of 0.5%, 1%, and 1.5% by weight. The results demonstrate a marked difference in the conductive behavior of scaffolds depending on the type and concentration of incorporated nanomaterials. Across all concentrations, AL-GQDs scaffolds exhibited significantly higher conductivity compared to their AL-GO counterparts, with all differences being statistically significant ($p < 0.001$). Specifically, at 0.5% loading, the conductivity of AL-GQDs scaffolds reached approximately 420 µS/cm, which is nearly five times higher than that of AL-GO scaffolds at the same concentration (80 µS/cm). This trend persisted at higher concentrations, where AL-GQDs scaffolds achieved values of 450 µS/cm and 500 µS/cm at 1% and 1.5%, respectively, whereas AL-GO scaffolds exhibited only modest increases to 90 µS/cm and 100 µS/cm.

The superior conductivity of AL-GQDs scaffolds can be attributed to the intrinsic quantum confinement and edge effects of GQDs, which impart unique electronic properties not present in larger GO nanosheets[57]. GQDs possess discrete energy levels and exhibit sp^2-hybridized carbon domains within their structure, facilitating efficient charge carrier mobility. Furthermore, the zero-dimensional spherical morphology of GQDs enables uniform dispersion throughout the hydrogel matrix, establishing continuous conductive pathways even at low concentrations[58]. In contrast, GO nanosheets, while structurally advantageous for mechanical reinforcement, possess oxygen-containing functional groups (epoxy, hydroxyl, and carboxyl) that disrupt π-conjugation across the graphene lattice, leading to significantly reduced electrical conductivity. Moreover, GO's large planar structure increases the likelihood of restacking and agglomeration, which impedes the formation of effective percolation networks essential for charge transport[59]. The incremental rise in conductivity with increasing GQDs concentration suggests the formation of a more interconnected conductive network, where higher filler content increases the number of contact points between adjacent GQDs, thus enhancing the percolation threshold[60]. However, the conductivity improvement in AL-GO scaffolds was minimal with increasing concentration, indicating that beyond a certain point, GO's contribution to electronic transport is limited by its inherent structural defects and insulating oxygen functionalities[61]. These findings are consistent with previous studies, which have reported the superior electroconductive properties of GQDs over GO in polymeric matrices. The pronounced difference in conductivity profiles underscores the critical role of nanomaterial dimensionality and surface chemistry in determining the electrical properties of composite scaffolds[61]. From an application perspective, the high conductivity of AL-GQDs scaffolds positions them as promising candidates for bioelectronic interfaces, neural tissue engineering, and electroactive tissue regeneration, where electrical stimulation plays a pivotal role in cellular behavior modulation. On the other hand, AL-GO scaffolds, with their moderate conductivity and superior mechanical properties, may be more suited for applications where structural support is prioritized over electronic functionality.

3.8. Cell proliferation

Figure 9a illustrates the cell viability (%) of C6 glioma cells cultured on tissue culture polystyrene (TCP), pure AL (No (nano particles) NPs), and AL-GONPs scaffolds

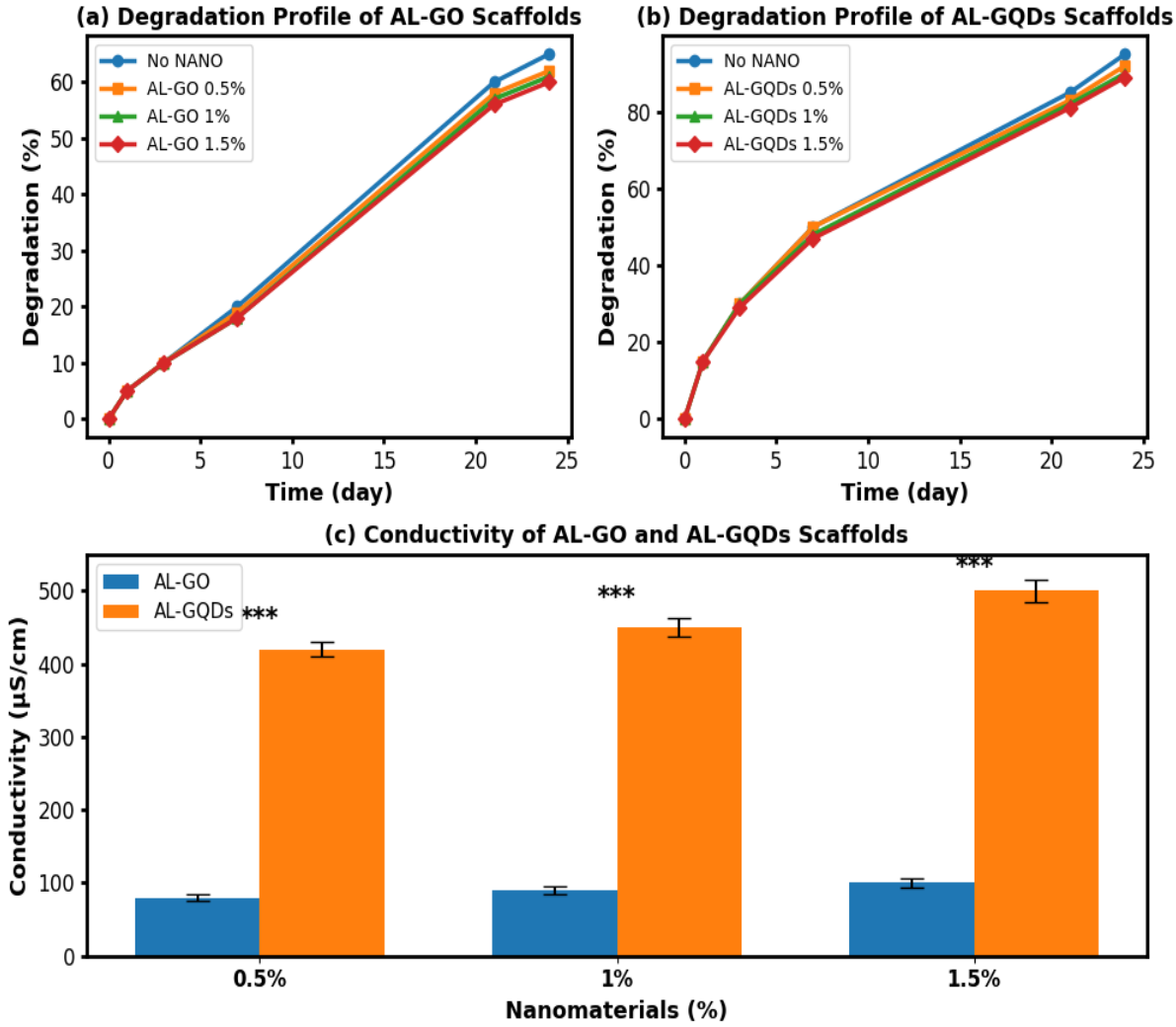

Figure 8. a) The degradation of AL-GO scaffolds, b) AL-GQDs scaffolds, and c) the conductivity of AL-GO and AL-GQDs scaffolds, ***p < 0.001 (n=3)

containing different concentrations of GO (0.5%, 1%, 1.5%) over 1, 3, and 7 days. A time-dependent increase in viability was observed across all groups, indicating sustained cellular adaptation and proliferation.

On day 1, all samples exhibited comparable viability levels, suggesting that the initial cell attachment was not significantly influenced by the presence of GO. However, by day 3 and day 7, scaffolds containing GO demonstrated a marked increase in viability compared to the TCP and No NPs controls. This enhancement was statistically significant ($p < 0.05$ to $p < 0.01$), particularly in scaffolds with 1% and 1.5% GO content. The improved cell viability in AL-GONPs scaffolds can be attributed to the bioactive surface chemistry of GO nanosheets, which enhance protein adsorption, promote cell adhesion, and modulate cytoskeletal organization[62]. Furthermore, the oxygenated functional groups on GO surfaces facilitate favorable interactions with extracellular matrix proteins, thereby improving the biocompatibility of the scaffold. The porous microarchitecture formed by the GO sheets also contributes to enhanced nutrient and oxygen diffusion, supporting cell survival and proliferation over time[63]. Figure 9b presents the proliferation profile of C6 cells cultured on TCP and AL-GONPs scaffolds in the presence (+) and absence (-) of BoNT/A. In the absence of BoNT/A (-), a progressive increase in proliferation was observed, with significant enhancements by day 3 and day 7 ($p < 0.001$). This indicates that the AL-GONPs scaffolds provide a supportive microenvironment that facilitates cell division and metabolic activity. Conversely, in BoNT/A-treated groups (+), a substantial reduction in cell proliferation was noted across all time points, with no significant difference compared to TCP controls. This inhibitory effect of BoNT/A on proliferation aligns with its known mechanism of action, where it interferes with vesicular exocytosis and downregulates neurogenic signaling pathways, thereby suppressing mitotic activity[64]. Importantly, despite the presence of GO in the

scaffolds, the BoNT/A-induced proliferation suppression was not reversed, indicating the dominant inhibitory effect of BoNT/A over scaffold-induced bioactivity[65].

Figure 9c depicts the cell viability profile of scaffolds incorporated with GQDs at varying concentrations (0.5%, 1%, 1.5%), alongside TCP and No NPs controls. Similar to AL-GONPs scaffolds, a time-dependent increase in viability was evident in all groups. However, the degree of enhancement in AL-GQDs scaffolds was slightly lower compared to AL-GONPs scaffolds at equivalent concentrations. The observed viability improvement in AL-GQDs scaffolds can be attributed to the unique physicochemical properties of GQDs, including their nanoscale dimensions, excellent dispersibility, and functional surface groups, which enhance cellular interactions[66]. Nevertheless, due to their zero-dimensional structure and limited surface area compared to GO nanosheets, the extent of cell-matrix interactions is relatively reduced, leading to a less pronounced viability enhancement[67]. This suggests that while GQDs contribute to scaffold biocompatibility, their role in promoting cellular adhesion and proliferation is less effective than GO when incorporated into a hydrogel matrix. Figure 9d demonstrates the proliferation behavior of C6 cells on AL-GQDs scaffolds with and without BoNT/A treatment. In the absence of BoNT/A (-), a substantial increase in proliferation was observed, reaching peak levels by day 3 ($p < 0.001$), followed by a slight plateau at day 7. This trend indicates that AL-GQDs scaffolds provide a favorable microenvironment for initial cell proliferation, which stabilizes over extended culture periods. In BoNT/A-treated groups (+), a significant reduction in proliferation was evident, mirroring the inhibitory effects observed in AL-GONPs scaffolds. Despite the unique quantum properties of GQDs, the presence of BoNT/A effectively suppressed cellular proliferation across all groups, confirming its dominant role in modulating cellular behavior through vesicular transport inhibition and synaptic signaling disruption[68]. While both AL-GONPs and AL-GQDs scaffolds enhanced proliferation in untreated conditions, the magnitude of proliferation was slightly higher in AL-GONPs scaffolds. This difference underscores the superior bioactivity of GO nanosheets in modulating cell-matrix interactions, likely due to their higher surface area and mechanical reinforcement properties that influence mechanotransduction pathways.

3.9. Gene expression

The comparative analysis of gene expression in C6 glioma cells cultured on AL-GO and AL-GQDs scaffolds provides significant insights into the interplay between scaffold architecture, mechanical properties, and cellular responses (Figure 10, Table 1). Despite the apparent simplicity of the experimental design, a deeper evaluation reveals critical mechanistic pathways through which scaffold composition modulates gene expression, thereby addressing existing challenges in neural tissue engineering. The expression levels of PLCB1 and TRPV1, two genes intricately involved in calcium signaling and neuronal plasticity, demonstrated distinct trends between the two scaffold types. AL-GO scaffolds exhibited markedly higher expression ratios for both PLCB1 (0.02) and TRPV1 (0.20) compared to AL-GQDs scaffolds (PLCB1: 0.015; TRPV1: 0.15), with statistical significance ($p < 0.01$). This upregulation can be directly correlated to the structural and surface chemistry attributes of GO, which are absent in GQDs. GO's two-dimensional, sheet-like morphology provides extensive contact interfaces with the AL matrix, enhancing the mechanical integrity of the scaffold (7 kPa) and establishing a continuous load-bearing network[69]. This robust mechanical framework facilitates mechanotransduction pathways, which are critical modulators of gene expression in neural cells. The mechanical cues transmitted via focal adhesion complexes activate downstream signaling cascades, including the phosphoinositide pathway (PLCB1 activation) and TRPV1-associated ion channel regulation, thereby promoting gene upregulation[70]. This mechanotransduction-induced gene expression is a fundamental mechanism that bridges scaffold biomechanics with cellular phenotype modulation[71]. In contrast, GQDs, owing to their zero-dimensional structure and limited lateral connectivity, fail to establish a comparable mechanical reinforcement within the hydrogel matrix, resulting in a significantly lower compressive strength (3 kPa)[72]. The diminished mechanical support translates into weaker focal adhesion formation and reduced activation of mechanosensitive genes[73]. Additionally, the smaller surface area of GQDs limits biointeractive sites necessary for efficient protein adsorption and integrin-mediated cell-scaffold anchorage, further contributing to the subdued gene expression profiles observed[74]. From a surface chemistry perspective, GO's abundant oxygen-containing functional groups (hydroxyl, epoxy, carboxyl) offer multiple binding sites that enhance hydrophilicity and promote extracellular matrix protein adsorption. These interactions facilitate stronger cell adhesion, enabling cytoskeletal organization and sustained signal transduction, which are essential for maintaining elevated expression of genes associated with cellular proliferation, differentiation, and neural response[75]. GQDs, despite their quantum confinement properties, lack the extensive surface functionalities and structural framework necessary to induce similar levels of cellular engagement[33]. The application of BoNT/A

across both scaffold systems consistently led to a downregulation of gene expression. This effect, however, was more pronounced in AL-GQDs scaffolds, indicating that the architectural and chemical limitations of GQDs exacerbate BoNT/A's inhibitory influence. In contrast, the superior mechanical and biochemical environment provided by AL-GO scaffolds mitigated, to some extent, the suppressive impact of BoNT/A on gene expression, underscoring GO's pivotal role in preserving cellular functionality even under neurotoxin-induced stress[76]. Furthermore, the biocompatibility profiles align coherently with the gene expression data. AL-GO scaffolds demonstrated enhanced cellular viability and proliferation in earlier assays, reinforcing the premise that a mechanically robust and biointeractive scaffold environment is instrumental in supporting not only cell survival but also functional gene expression. While the overall design of this study may appear straightforward, the findings elucidate critical scaffold–cell interactions that are often underexplored in more complex systems. By systematically correlating scaffold mechanical properties and surface chemistry with gene expression outcomes, this work offers a mechanistic foundation that bridges material design with functional cellular behavior. Such insights are essential for the rational design of next-generation scaffolds aimed at neural tissue regeneration, where fine-tuning mechanical cues and biochemical interfaces is vital for achieving therapeutic efficacy. These findings, although derived from a targeted model system, provide generalizable principles applicable to a broader spectrum of biomaterial–cell interactions. The scaffold-dependent modulation of BoNT/A's biological effects further amplifies the translational potential of this platform for neuroregenerative applications where controlled gene expression is a therapeutic requisite.

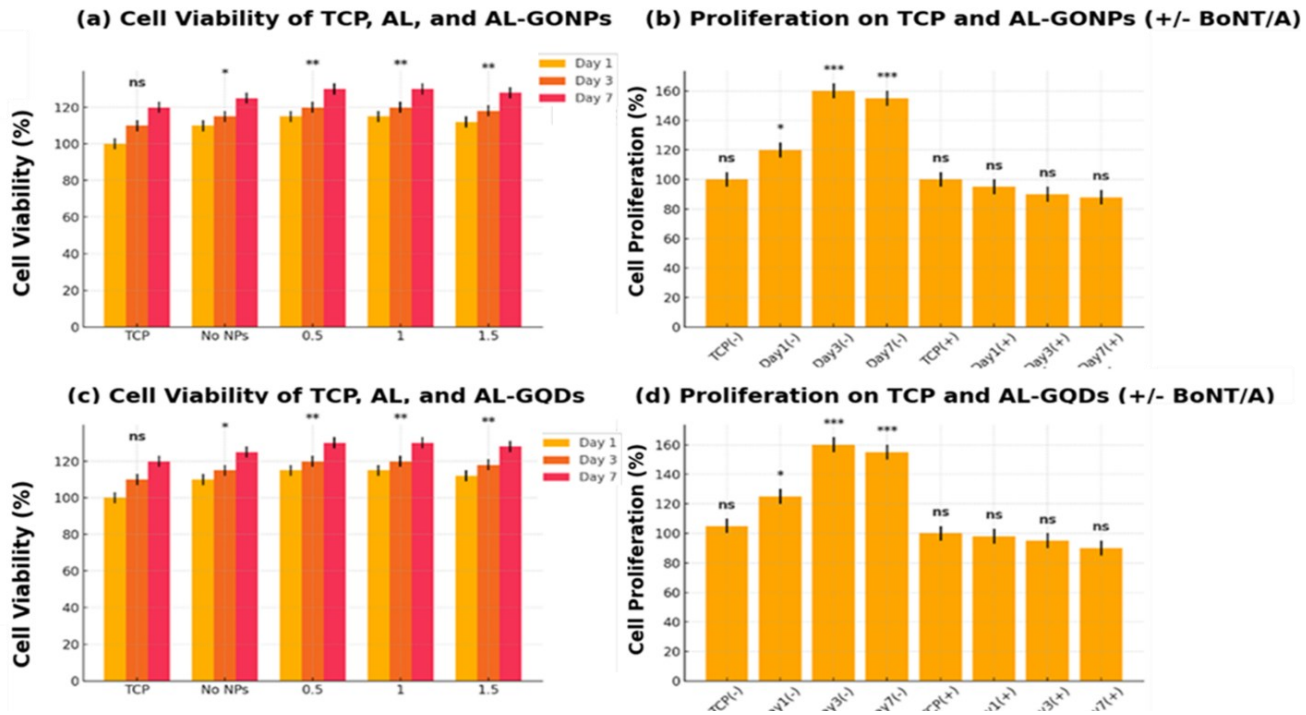

Figure 9. Cellular evaluation of scaffolds through viability and proliferation assays. a) Cell viability (%) of C6 glioma cells cultured on TCP, pure AL, and AL-GONPs scaffolds at 0.5%, 1%, and 1.5% GO concentrations after 1, 3, and 7 days. Significant increases in cell viability were observed in AL-GONPs scaffolds compared to controls (*$p < 0.05$, **$p < 0.01$). b) Proliferation profile of C6 cells on TCP and AL-GONPs scaffolds in the presence (+) and absence (−) of BoNT/A. A substantial proliferation enhancement was observed in BoNT/A-untreated groups by day 3 and day 7 (***$p < 0.001$), while BoNT/A treatment resulted in marked proliferation suppression (ns, not significant). c) Cell viability (%) of C6 glioma cells on TCP, AL, and AL-GQDs scaffolds (0.5%, 1%, 1.5%) over 1, 3, and 7 days, with significant improvements compared to controls (*$p < 0.05$, **$p < 0.01$). d) Proliferation analysis on TCP and AL-GQDs scaffolds in the presence (+) and absence (−) of BoNT/A. BoNT/A-untreated scaffolds exhibited significantly higher proliferation on day 3 and day 7 (***$p < 0.001$), while BoNT/A treatment suppressed proliferation to control levels (ns). Error bars represent standard deviation ($n = 3$). Statistical significance was determined using independent t-tests

doi 0.57647/pibm.2025.1403.36

Table 1. Comparative Summary of Scaffold Gene Expression and Related Properties

Scaffold Type	TRPV1 Expression (Ratio)	PLCB1 Expression (Ratio)	Effect of BoNT/A on Gene Expression	Mechanical Strength (kPa)	Biocompatibility	Key Observations	Porosity (%) at 1.5 wt%	Swelling ratio (%) at 1.5 wt%	Conductivity (µS/cm) at 1.5 wt%
AL-GO	0.2	0.02	Decreased	7	High	Higher compressive strength and hydrophilic properties support better cell adhesion and gene expression.	110	740	100
AL-GQDs	0.15	0.015	Decreased	3	Very high	Smaller size and zero-dimensional structure led to lower mechanical reinforcement while maintaining favorable cellular interactions and enhanced electrical properties.	137	670	500

3.10. Cell Attachment

Figure 11 presents a SEM image showcasing the microstructural architecture of the AL-GO scaffold after culturing with C6 glioma cells. The image reveals a highly porous, interconnected network with irregular pore morphologies and heterogeneous surface topography, which are critical parameters in designing biomimetic scaffolds for neural tissue engineering. The observed pore diameters, ranging between 10–30 µm, fall within the optimal size range to facilitate cellular infiltration, nutrient diffusion, and waste removal. More importantly, the presence of well-distributed micro- and nanopores enhances the scaffold's surface area, providing ample anchorage points for cell adhesion molecules (e.g., integrins). The rough, wrinkled texture of the pore walls, attributed to the incorporation of GO nanosheets, introduces nano-topographical cues that are essential for focal adhesion complex formation and subsequent cytoskeletal organization[77]. Notably, multiple filopodia-like cellular extensions can be observed penetrating into the scaffold matrix, indicating active cell–material interactions. These extensions suggest robust cellular anchorage and spreading behavior, which is a direct consequence of the scaffold's mechanical stability and surface chemistry[78]. The two-dimensional lamellar structure of GO not only reinforces the mechanical framework but also offers abundant oxygen-containing functional groups, which enhance hydrophilicity and promote protein adsorption at the cell-scaffold interface. This biomolecular conditioning of the scaffold surface facilitates integrin clustering and activates mechanotransduction pathways that regulate cell proliferation, differentiation, and gene expression[79]. Furthermore, the irregular distribution of pore sizes and the multi-scale roughness observed in the SEM image are highly advantageous for mimicking the native extracellular

matrix (ECM) microenvironment. Such structural heterogeneity supports dynamic cell-matrix interactions and promotes the development of tissue-specific architectures. This is particularly critical in neural tissue engineering, where scaffold microarchitecture must accommodate neurite outgrowth and synaptic connectivity[80]. From a functional standpoint, the intricate porous network and the nanoscale features introduced by GO incorporation enhance not only cell adhesion but also mechanosensitive signaling, which are key drivers for downstream biological responses. The morphological evidence presented in this SEM image substantiates the scaffold's capability to support cellular viability and function, as observed in previous biological assays. In conclusion, the SEM analysis of the AL-GO scaffold confirms that its hierarchical porous architecture, combined with nanoscale surface roughness and functional group-rich chemistry, provides a conducive microenvironment for effective cell–scaffold integration. These structural attributes are fundamental in driving cell adhesion, mechanotransduction, and ultimately, tissue regeneration efficacy.

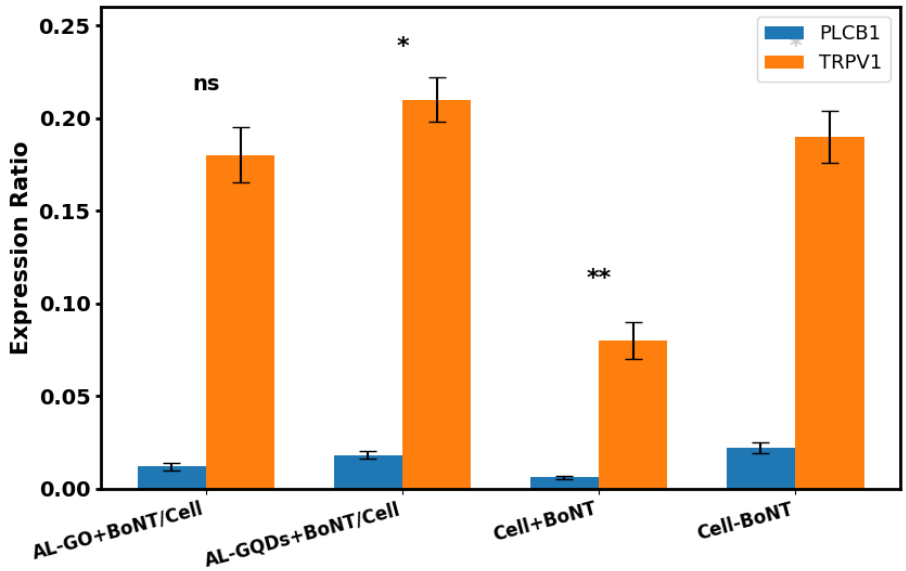

Figure 10. Gene expression analysis of C6 glioma cells cultured on AL-GO and AL-GQDs scaffolds in the presence (+) and absence (−) of BoNT/A. The expression ratios of PLCB1 and TRPV1 were quantified using qPCR, normalized against GAPDH, and presented as mean ± standard deviation (n = 3). Significant differences were observed in TRPV1 expression between AL/−BoNT/Cell and AL/+BoNT/Cell (*$p < 0.05$), as well as between Cell/−BoNT and Cell/+BoNT (**$p < 0.01$). No significant difference (ns) was noted in PLCB1 expression between AL/−BoNT/Cell and ALG/+BoNT/Cell. The results indicate that scaffold composition and BoNT/A exposure synergistically modulate gene expression, with GO-based scaffolds exhibiting enhanced resilience against BoNT/A-induced downregulation (n=3)

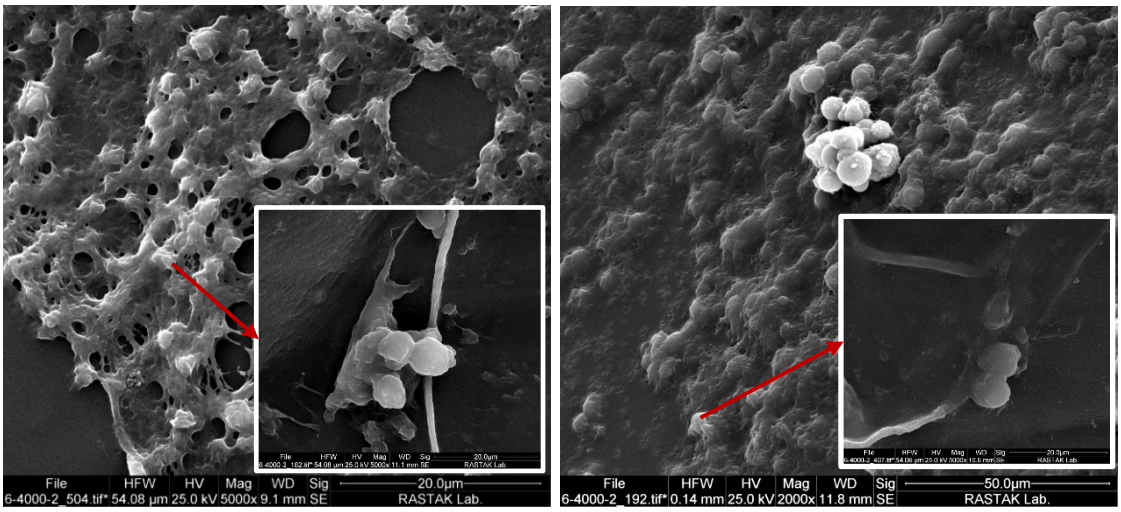

a b

Figure 11. SEM image of C6 cells in the presence of a: AL-GO and b: AL-GQDs. Scale bar in a; 20 µm. Scale bar in b; 50 µm

doi 0.57647/pibm.2025.1403.36

4. Future perepective and conclusion

4.1. Future perepective

While the current study successfully demonstrates the potential of GO and GQDs-incorporated alginate-based scaffolds in modulating cellular behavior, enhancing mechanical integrity, and influencing gene expression, several avenues remain open for further exploration to maximize the translational impact of these findings. The fundamental insights derived from this work provide a robust platform for advancing scaffold design strategies toward more complex and application-specific biomedical solutions. One of the primary limitations of the present study lies in the evaluation of scaffold performance under simplified in vitro conditions using a single cell type (C6 glioma cells). Although these models offer a controlled environment for mechanistic investigations, they inherently lack the biological complexity of native tissue microenvironments. Future studies should focus on validating these scaffolds in 3D co-culture systems that incorporate multiple cell types, such as neurons, astrocytes, and endothelial cells, to better mimic the cellular heterogeneity and dynamic interactions present in neural tissues. Moreover, while GO and GQDs have been individually assessed for their respective roles in reinforcing mechanical properties and enhancing scaffold conductivity, the synergistic incorporation of both nanomaterials within a single scaffold matrix remains unexplored. Hybridizing the high mechanical strength of GO with the superior electrical conductivity of GQDs could lead to multifunctional scaffolds capable of providing both structural support and bioelectrical cues, which are essential for applications such as neural regeneration and electroactive tissue engineering. Another promising direction involves the functionalization of GO and GQDs with bioactive ligands or peptides to further augment cell-scaffold interactions at the molecular level. Functional groups such as RGD peptides or growth factor-mimicking sequences could be conjugated to the nanomaterials to enhance integrin-mediated adhesion and promote lineage-specific differentiation. In addition, although BoNT/A was utilized in this study as a model bioactive molecule to assess scaffold-mediated gene modulation, the exploration of other pharmacological agents or gene delivery systems integrated within the scaffold could significantly broaden the therapeutic applications. Incorporating controlled release systems or stimulus-responsive elements would allow for dynamic regulation of the scaffold's biological activity in response to the tissue microenvironment. From a materials engineering perspective, the current freeze-drying fabrication method offers simplicity and efficacy in generating porous scaffolds. However, advanced biofabrication techniques such as 3D bioprinting or electrospinning of nanofibrous composites could be employed to achieve more precise control over scaffold architecture, porosity gradients, and anisotropy, thereby enhancing functional integration with host tissues. While the study has been conducted using conventional GO and GQDs synthesis approaches, recent advancements in green synthesis methods leveraging eco-friendly precursors could be explored to enhance the biocompatibility and scalability of these nanomaterials for clinical translation.

In conclusion, the findings of this research lay a solid foundation for scaffold-based strategies in neural tissue engineering, highlighting the critical role of scaffold architecture and nanomaterial properties in guiding cellular responses. Building upon these results, future investigations should aim to integrate multi-scale material design, advanced biofunctionalization, and dynamic biological modeling to develop next-generation intelligent scaffolds that bridge the gap between laboratory research and clinical application.

4.2. Conclusion

This study successfully developed and evaluated alginate-based scaffolds incorporated with GO and GQDs for neural tissue engineering applications, focusing on the interplay between scaffold composition, mechanical properties, and cellular responses. A comprehensive set of physicochemical, mechanical, and biological assays was conducted to elucidate the structure–function relationship of these nanocomposite scaffolds. Morphological analyses confirmed that the incorporation of GO introduced a highly porous, interconnected microstructure with nanoscale surface roughness, facilitating effective cell adhesion and infiltration. Scaffolds containing GQDs exhibited higher porosity levels; however, their smoother surface topography resulted in less efficient focal adhesion formation compared to GO-based scaffolds. The distinct architectural differences directly influenced the scaffold's mechanical properties, where AL-GO scaffolds exhibited a compressive strength of 7 kPa, significantly higher than AL-GQDs scaffolds (3 kPa, $*p < 0.001$). This mechanical reinforcement in AL-GO scaffolds is attributed to the two-dimensional lamellar structure of GO, which forms a continuous load-bearing network within the hydrogel matrix. Swelling and degradation assessments demonstrated that both scaffold types exhibited desirable swelling capacities, with AL-GO scaffolds showing higher swelling ratios due to their hydrophilic functional groups. The degradation rates were found to be time-dependent, with AL-GQDs scaffolds exhibiting faster degradation profiles, whereas AL-GO scaffolds maintained structural stability over an extended period, making them more suitable for long-term tissue regeneration applications.

doi: 10.57647/pibm.2025.1403.36

Electrical conductivity measurements revealed that AL-GQDs scaffolds provided superior conductivity (~500 µS/cm at 1.5 wt%) compared to AL-GO scaffolds (~100 µS/cm), highlighting their potential utility in applications where bioelectrical signaling is critical. Cell viability and proliferation assays (MTT) confirmed that both AL-GO and AL-GQDs scaffolds supported high levels of cell viability, exceeding 120% by day 7. However, AL-GO scaffolds consistently outperformed AL-GQDs scaffolds in supporting sustained cell proliferation, particularly under challenging conditions induced by BoNT/A exposure. The presence of BoNT/A resulted in a significant decrease in proliferation across all groups, but AL-GO scaffolds exhibited a reduced magnitude of suppression, indicating their potential to maintain cellular functionality under neurotoxic stress. Gene expression analyses of PLCB1 and TRPV1 provided further insights into the scaffold-induced modulation of cellular responses. AL-GO scaffolds demonstrated significantly higher expression ratios of both genes (PLCB1: 0.02; TRPV1: 0.20) compared to AL-GQDs scaffolds (PLCB1: 0.015; TRPV1: 0.15), with statistical significance (*p < 0.05 to *$p < 0.01$). These findings highlight the pivotal role of scaffold mechanical integrity and nano-topographical features in activating mechanotransduction pathways that regulate neural-related gene expression. SEM imaging corroborated these molecular findings, where C6 cells cultured on AL-GO scaffolds exhibited enhanced adhesion, spreading, and cytoplasmic extensions anchored firmly within the scaffold network. In contrast, AL-GQDs scaffolds, while supporting cell attachment, showed reduced cellular anchorage and spreading due to their smoother surface morphology and lower mechanical strength.

Overall, this study delineates the critical influence of scaffold architecture and nanomaterial selection on cellular behavior at both morphological and genetic levels. While GO provided superior mechanical reinforcement and biointeractive surfaces, GQDs contributed to scaffold porosity and conductivity but lacked structural interconnectivity. The differential performance of these nanomaterials underscores the importance of tailored scaffold design in modulating specific biological outcomes for tissue engineering applications.

The foundational insights derived from this work establish AL-GO nanocomposite scaffolds as promising candidates for neural tissue engineering, with potential for further optimization through advanced biofunctionalization, hybrid nanomaterial integration, and dynamic in vivo modeling. These findings not only reinforce the significance of material–cell interaction strategies but also pave the way for the development of next-generation intelligent scaffolds with enhanced regenerative capabilities.

Data availability

The datasets used and/or analysed during the current study available from the corresponding author on reasonable request.

Conflict of Interest

The authors declare have no competing interests as defined by Nature Research, or other interests that might be perceived to influence the results and/or discussion reported in this paper.

Funding

None

Authors contributions
All authors contributed equally to the conception, design, execution, and writing of this work. All authors read and approved the final manuscript.

Availability of data and materials
The datasets generated during and/or analyzed during the current study are available from the corresponding author on reasonable request.

Conflict of interests
The authors declare that they have no known competing financial interests or personal relationships that could have appeared to influence the work reported in this paper.

Reference

[1] Mohanaraman, S. P. and Chidambaram, R. 2024. Heliyon Review article A holistic review on red fluorescent graphene quantum dots , its synthesis , unique properties with emphasis on biomedical applications Ultraviolet irradiation. *Heliyon*, 10(16), p. e35760.
DOI: https://doi.org/10.1016/j.heliyon.2024.e35760

[2] Pourmadadi, M. et al. 2024. Green Synthesis of pH-Sensitive Carboxymethyl Cellulose/Agarose/Carbon Quantum Dots Nanocarriers for Quercetin Delivery to A549 Lung Cancer Using an Emulsification Method. *Bionanoscience*, 14(4), pp. 4570–4584.
DOI: https://doi.org/10.1007/s12668-024-01426-9

[3] Shahnaz, T. et al. 2024. Graphene-based nanoarchitecture as a potent cushioning / filler in polymer composites and their applications. J. *Mater. Res. Technol.*, 28, pp. 2671–2698.
DOI: https://doi.org/10.1016/j.jmrt.2023.12.108

[4] Farjaminejad, S. et al. 2024. Advances and Challenges in Polymer-Based Scaffolds for Bone Tissue Engineering: A Path Towards Personalized Regenerative Medicine. *Polymers*, 16(23).
DOI: https://doi.org/10.3390/polym16233303

[5] Yang, X. et al. 2021. Graphene Oxide Quantum Dots Promote Osteogenic Differentiation of Stem Cells from Human Exfoliated Deciduous Teeth via the Wnt/β-Catenin Signaling Pathway. *Stem Cells Int.*, 2021.

DOI: https://doi.org/10.1155/2021/8876745

[6] Geng, B. et al. 2021. Surface charge-dependent osteogenic behaviors of edge-functionalized graphene quantum dots. *Chem. Eng. J.*, 417, p. 128125.
DOI: https://doi.org/10.1016/J.CEJ.2020.128125

[7] Si, R., Gao, C., Guo, R., Lin, C., Li, J. and Guo, W. 2020. Human mesenchymal stem cells encapsulated-coacervated photoluminescent nanodots layered bioactive chitosan/collagen hydrogel matrices to indorse cardiac healing after acute myocardial infarction. J. *Photochem. Photobiol. B Biol*., 206, p. 111789.
DOI: https://doi.org/10.1016/J.JPHOTOBIOL.2020.111789

[8] Hou, T., Ma, H., Gao, X., Sun, H., Wang, L. and An, M. 2022. Study on Long-Term Tracing of Fibroblasts on Three-Dimensional Tissue Engineering Scaffolds Based on Graphene Quantum Dots. *Int. J. Mol. Sci.*, 23(19).
DOI: https://doi.org/10.3390/ijms231911040

[9] Joy, A., Megha, M., Mohan, C. C., Thomas, J., Bhat, S. G. and Muthuswamy, S. 2024. Novel polycaprolactone-based biomimetic grafts enriched with graphene oxide and cerium oxide: Exploring improved osteogenic potential. *Mater. Today Chem*., 37, p. 102031.
DOI: https://doi.org/10.1016/J.MTCHEM.2024.102031

[10] Prakash, J., Prema, D., Venkataprasanna, K. S., Balagangadharan, K., Selvamurugan, N. and Venkatasubbu, G. D. 2020. Nanocomposite chitosan film containing graphene oxide/hydroxyapatite/gold for bone tissue engineering. *Int. J. Biol. Macromol*., 154, pp. 62–71.
DOI: https://doi.org/10.1016/J.IJBIOMAC.2020.03.095

[11] Bagas, M. et al. 2025. ChemPhysMater 3D printed 2D materials for tissue engineering applications. *ChemPhysMater*, 4(3), pp. 251–273.
DOI: https://doi.org/10.1016/j.chphma.2024.12.004

[12] Wu, H., Huang, Q. and Tan, Y. 2019. *Carbon nanomaterials for biomedical applications. in Carbon Nanomaterials: Modeling, Design, and Applications*, pp. 255–293
DOI: https://doi.org/10.1201/9781351123587-7

[13] Motiee, E. S., Karbasi, S., Bidram, E. and Sheikholeslam, M. 2023. Investigation of physical, mechanical and biological properties of polyhydroxybutyrate-chitosan/graphene oxide nanocomposite scaffolds for bone tissue engineering applications. *Int. J. Biol. Macromol*., 247, p. 125593.
DOI: https://doi.org/10.1016/J.IJBIOMAC.2023.125593

[14] Purohit, S. D., Bhaskar, R., Singh, H., Yadav, I., Gupta, M. K. and Mishra, N. C. 2019. Development of a nanocomposite scaffold of gelatin–alginate–graphene oxide for bone tissue engineering. *Int. J. Biol. Macromol*., 133, pp. 592–602.
DOI: https://doi.org/10.1016/J.IJBIOMAC.2019.04.113

[15] Méndez-Lozano, N., Pérez-Reynoso, F. and González-Gutiérrez, C. 2022. Eco-Friendly Approach for Graphene Oxide Synthesis by Modified Hummers Method. *Materials (Basel)*., 15(20).
DOI: https://doi.org/10.3390/ma15207228

[16] Facure, M. H. M., Schneider, R., Mercante, L. A. and Correa, D. S. 2022. Rational hydrothermal synthesis of graphene quantum dots with optimized luminescent properties for sensing applications. *Mater. Today Chem.*, 23, p. 100755.
DOI: https://doi.org/10.1016/J.MTCHEM.2021.100755

[17] Janarthanan, G., Pillai, M. M., Kulasekaran, S. S., Rajendran, S. and Bhattacharyya, A. 2020. Engineered knee meniscus construct: understanding the structure and impact of functionalization in 3D environment. *Polym. Bull*., 77(5), pp. 2611–2629.
DOI: https://doi.org/10.1007/S00289-019-02874-0/METRICS

[18] Pourmadadi, M. et al. 2025. Development of Poly(ether sulfone)/Poly(vinyl alcohol)/Magnesium-Doped Carbon Quantum Dot Scaffolds for Bone Tissue Engineering. *ACS Biomater. Sci. Eng*..
DOI: https://doi.org/10.1021/acsbiomaterials.4c02124

[19] Abedi, S., Mohajeri, A., Benisi, S. Z., Pezeshki-Modaress, M. and Shabestari, S. M. 2025. Three-dimensional nanofibrous PCL/gelatin scaffold fabricated using centrifugal force assisted wet electrospinning technique. *Sci. Rep*., 15(1), pp. 1–24.
DOI: https://doi.org/10.1038/s41598-025-20814-z

[20] Pourmadadi, M., Fallahi, F., Alesheikh, M. and Mohammadi, S. 2025. In vitro evaluation of bioinspired PEC / Zein / ZnO nanocarriers for pH-responsive curcumin delivery in colorectal cancer therapy. *Carbohydr. Polym. Technol. Appl*., 12, p. 101044.
DOI: https://doi.org/10.1016/j.carpta.2025.101044

[21] Pereira Junior, A. A. M., dos Santos, F. K. F., de Almeida Araújo, F., Leite-Barbosa, O. S., Altoé, L. and da Veiga Junior, V. F. 2025. Chemical and Structural Analysis of Graphene Oxide Reduced with Naringenin: A Natural Product-Based Alternative. *J. Mater. Res. Technol.*, 37, pp. 2850–2865.
DOI: https://doi.org/10.1016/j.jmrt.2025.06.173

[22] Liu, C. 2024. From Preparation and Modification Methods to Application. J. *Carbon Res*., 10(7), pp. 1–40.

[23] Eda, G. and Chhowalla, M. 2010. Chemically derived graphene oxide: Towards large-area thin-film electronics and optoelectronics. *Adv. Mater*., 22(22), pp. 2392–2415.
DOI: https://doi.org/10.1002/ADMA.200903689

[24] Sohal, N., Singla, S., Malode, S. J., Basu, S., Maity, B. and Shetti, N. P. 2023. Bioresource-Based Graphene Quantum Dots and Their Applications: A Review. *ACS Appl. Nano Mater*., 6(13), pp. 10925–10943.
DOI: https://doi.org/10.1021/ACSANM.3C02185/ASSET/IMAGES/MEDIUM/AN3C02185_0013.GIF

[25] Bi, Y., Xie, S., Li, Z., Dong, S. and Teng, L. 2025. Precise nanoscale fabrication technologies, the 'last mile' of medicinal development. *Acta Pharmaceutica Sinica B*, 15(5), pp. 2372–2401.
DOI: https://doi.org/10.1016/j.apsb.2025.03.040

[26] Shabestari, S. M. et al. 2025. Role phosphate-modified cellulose into the scaffold based on poly (glycerol azelaic acid)-co-poly(ε-caprolactone) for using bone regenerative medicine. *Int. J. Biol. Macromol*., p. 140855.
DOI: https://doi.org/10.1016/j.ijbiomac.2025.140855

[27] Saito, K., Xu, T. and Ishikita, H. 2022. Correlation between C•O Stretching Vibrational Frequency and p KaShift of Carboxylic Acids. *J. Phys. Chem. B*, 126(27), pp. 4999–5006.
DOI: https://doi.org/10.1021/acs.jpcb.2c02193

[28] Gonzaga, M. L. C., Menezes, T. M. F., De Souza, J. R. R., Ricardo, N. M. P. S. and Soares, S. D. A. 2013. Structural characterization of β glucans isolated from Agaricus blazei Murill using NMR and FTIR spectroscopy. *Bioact. Carbohydrates Diet. Fibre*, 2(2), pp. 152–156.
DOI: https://doi.org/10.1016/J.BCDF.2013.10.005

[29] Shabestari, S. M. et al. 2025. pH-Responsive Chitosan-Sodium Alginate Nanocarriers for Curcumin Delivery Against Brain Cancer. *Colloids Surfaces B Biointerfaces*, p. 114875.
DOI: https://doi.org/10.1016/j.colsurfb.2025.114875

[30] Hosseini, S. A., Mashaykhi, S. and Babaei, S. 2016. Graphene oxide/zinc oxide nanocomposite: A superior adsorbent for removal of methylene blue statistical analysis by response surface methodology (rsm). *South African J. Chem*., 69, pp. 105–112.
DOI: https://doi.org/10.17159/0379-4350/2016/v69a13

[31] Yuan, X., Liu, Z., Guo, Z., Ji, Y., Jin, M. and Wang, X. 2014. Cellular distribution and cytotoxicity of graphene quantum dots with different functional groups. *Nanoscale Res. Lett*., 9(1), pp. 1–9.
DOI: https://doi.org/10.1186/1556-276X-9-108

[32] Moreno, M., Sánchez Arribas, A., Royano, S., Izquierdo, Y. and Chicharro, M. 2024. Electroanalytical application of phenol-functionalized reduced graphene oxide produced using gallic acid in a single step. *FlatChem*, 44.
DOI: https://doi.org/10.1016/j.flatc.2023.100605

[33] Mirzaei, H., Ehsani, M. H. and Shakeri, A. 2025. Development and characterization of a graphene quantum dot/g-C_3N_4 photocatalyst for efficient degradation of Rhodamine B. *Sci. Rep*., 15(1), pp. 1–19.
DOI: https://doi.org/10.1038/s41598-025-13373-w

[34] Ghaffarkhah, A. et al. 2022. Synthesis, Applications, and Prospects of Graphene Quantum Dots: A Comprehensive Review. *Small*, 18(2).
DOI: https://doi.org/10.1002/SMLL.202102683

[35] Benedetti, M., Plessis, A., Ritchie, R. O., Dallago, M., Razavi, N. and Berto, F. 2021. Materials Science & Engineering R Architected cellular materials : A review on their mechanical properties towards fatigue-tolerant design and fabrication. *Mater. Sci. Eng. R*, 144, p. 100606.
DOI: https://doi.org/10.1016/j.mser.2021.100606

[36] He, M., Zhang, R., Zhang, K., Liu, Y., Su, Y. and Jiang, Z. 2019. Reduced graphene oxide aerogel membranes fabricated through hydrogen bond mediation for highly efficient oil/water separation. *J. Mater. Chem. A*, 7(18), pp. 11468–11477.
DOI: https://doi.org/10.1039/C9TA01700C

[37] Dhairiyasamy, R., Gabiriel, D., Varshney, D. and Singh, S. 2025. Optimizing nanomaterial dosages in concrete for structural applications using experimental design techniques. *Sci. Rep*., 15(1), pp. 1–20.
DOI: https://doi.org/10.1038/s41598-025-05265-w

[38] Wang, Y. et al. 2025. Progress in Research on Metal Ion Crosslinking Alginate-Based Gels. *Gels*, 11(1).
DOI: https://doi.org/10.3390/gels11010016

[39] Zeng, M. et al. 2025. Nacre-inspired graphene oxide/chitosan supported Pd species composite paper-like membrane with superior catalytic performance. *Int. J. Biol. Macromol*., 306, p. 141512.
DOI: https://doi.org/10.1016/J.IJBIOMAC.2025.141512

[40] El-husseiny, H. M., Mady, E. A., Hamabe, L. and Abugomaa, A. 2022. Materials Today Bio Smart / stimuli-responsive hydrogels : Cutting-edge platforms for tissue engineering and other biomedical applications. *Mater. Today Bio*, 13, p. 100186.
DOI: https://doi.org/10.1016/j.mtbio.2021.100186

[41] Jiang, H. et al. 2024. Surface strengthening mechanism of graphene-oxide membrane and its modified aluminium lamina under penetration loading. *Carbon N. Y*., 225, p. 119098.
DOI: https://doi.org/10.1016/J.CARBON.2024.119098

[42] Kurniawan, D., Weng, R., Chen, Y., Rahardja, M. R., Nanaricka, Z. C. and Chiang, W. 2022. Recent advances in the graphene quantum dot-based biological and environmental sensors. *Sensors and Actuators Reports*, 4, p. 100130.
DOI: https://doi.org/10.1016/j.snr.2022.100130

[43] Li, W. and Luo, P. 2025. Preparation and Performance Evaluation of Graphene Oxide-Based Self-Healing Gel for Lost Circulation Control. pp. 1–14.

[44] Luo, Y., Dong, B., Yang, H., Qiu, F., Yan, B. and Shu, S. 2024. Research progress on nanoparticles reinforced magnesium alloys. *J. Mater. Res. Technol*., 30, pp. 5166–5191.
DOI: https://doi.org/10.1016/j.jmrt.2024.04.129

[45] Pablos, J. L., Lozano, D., Manzano, M. and Vallet-regí, M. 2024. Materials Today Bio Regenerative medicine : Hydrogels and mesoporous silica nanoparticles. *Mater. Today Bio*, 29, p. 101342.
DOI: https://doi.org/10.1016/j.mtbio.2024.101342

[46] Hussain, S. and Maktedar, S. S. 2023. Results in Chemistry Structural , functional and mechanical performance of advanced Graphene-based composite hydrogels. *Results Chem*., 6, p. 101029.
DOI: https://doi.org/10.1016/j.rechem.2023.101029

[47] Alabi, A., Aubry, C. and Zou, L. 2022. Graphene Oxide-alginate Hydrogel for Drawing Water through an Osmotic Membrane. *ACS Omega*, 7(43), pp. 38337–38346.
DOI: https://doi.org/10.1021/acsomega.2c03138

[48] Bharathi, G., Nataraj, D., Premkumar, S. and Sowmiya, M. 2017. Graphene Quantum Dot Solid Sheets : Strong blue-light-emitting. *Sci. Rep*., pp. 1–17.
DOI: https://doi.org/10.1038/s41598-017-10534-4

[49] De France, K. J., Hoare, T. and Cranston, E. D. 2017. Review of Hydrogels and Aerogels Containing Nanocellulose. *Chem. Mater*., 29(11), pp. 4609–4631.
DOI: https://doi.org/10.1021/acs.chemmater.7b00531

[50] Xie, F., Gao, C. and Avérous, L. 2024. Alginate-based materials: Enhancing properties through multiphase formulation design and processing innovation. *Materials Science and Engineering R: Reports*, 159.
DOI: https://doi.org/10.1016/j.mser.2024.100799

[51] Kalluri, A., Dharmadhikari, B., Debnath, D., Patra, P. and Kumar, C. V. 2023. Advances in Structural Modifications and Properties of Graphene Quantum Dots for Biomedical Applications. *ACS Omega*, 8(24), pp. 21358–21376.
DOI: https://doi.org/10.1021/acsomega.2c08183

[52] Dananjaya, V., Marimuthu, S., Chunhui, R., Grace, N. and Abeykoon, C. 2024. Progress in Materials Science Synthesis , properties , applications , 3D printing and machine learning of graphene quantum dots in polymer nanocomposites. *Prog. Mater. Sci.*, 144, p. 101282. DOI: https://doi.org/10.1016/j.pmatsci.2024.101282

[53] Ge, R., Huo, T., Gao, Z., Li, J. and Zhan, X. 2023. GO-Based Membranes for Desalination. *Membranes*, 13(2). DOI: https://doi.org/10.3390/membranes13020220

[54] Henna, T. K. and Pramod, K. 2020. Graphene quantum dots redefine nanobiomedicine. *Materials Science and Engineering C*, 110. DOI: https://doi.org/10.1016/j.msec.2020.110651

[55] Dezfuli, A. S., Kohan, E., Fateh, S. T., Alimirzaei, N., Arzaghi, H. and Hamblin, M. R. 2021. RSC Advances preparation and surface engineering. *RSC Adv.*, 11, pp. 2253–2291. DOI: https://doi.org/10.1039/D0RA08041A

[56] Singh, R., Rawat, H., Kumar, A. and Gandhi, Y. 2024. Heliyon Graphene and its hybrid nanocomposite : A Metamorphoses elevation in the field of tissue engineering. *Heliyon*, 10(13), p. e33542. DOI: https://doi.org/10.1016/j.heliyon.2024.e33542

[57] Li, Y., Shu, H., Niu, X. and Wang, J. 2015. Electronic and Optical Properties of Edge-Functionalized Graphene Quantum Dots and the Underlying Mechanism. *J. Phys. Chem. C*, 119(44), pp. 24950–24957. DOI: https://doi.org/10.1021/ACS.JPCC.5B05935/SUPPL_FILE/JP5B05935_SI_001.PDF

[58] Zeng, Z. et al. 2018. Unraveling the cooperative synergy of zero-dimensional graphene quantum dots and metal nanocrystals enabled by layer-by-layer assembly. *J. Mater. Chem. A*, 6(4), pp. 1700–1713. DOI: https://doi.org/10.1039/C7TA09119B

[59] Eigler, S. and Dimiev, A. M. 2016. Functionalization and Reduction of Graphene Oxide. in *Graphene Oxide Fundam. Appl.*, pp. 175–229. DOI: https://doi.org/10.1002/9781119069447.CH6

[60] Seibert, J. R., Keleş, Ö., Wang, J. and Erogbogbo, F. 2019. Infusion of graphene quantum dots to modulate thermal conductivity and dynamic mechanical properties of polymers. *Polymer (Guildf)*, 185, p. 121988. DOI: https://doi.org/10.1016/J.POLYMER.2019.121988

[61] Huang, P. et al. 2021. Graphene film for thermal management: A review. *Nano Mater.* Sci., 3(1), pp. 1–16. DOI: https://doi.org/10.1016/j.nanoms.2020.09.001

[62] Guo, J., Cao, G., Wei, S., Han, Y. and Xu, P. 2023. Heliyon Progress in the application of graphene and its derivatives to osteogenesis. *Heliyon*, 9(11), p. e21872. DOI: https://doi.org/10.1016/j.heliyon.2023.e21872

[63] Ryon, S. et al. 2016. Graphene-based materials for tissue engineering Graphical Abstract HHS Public Access. *Adv Drug Deliv Rev*, 105, pp. 255–274. DOI: https://doi.org/10.1016/j.addr.2016.03.007

[64] Rahmatipour, H., Shabestari, S. M., Benisi, S. Z. and Samadikhah, H. 2025. Jo ur na l P re. *HELIYON*, p. e42350. DOI: https://doi.org/10.1016/j.heliyon.2025.e42350

[65] Lin, Y. H., Chiang, B. J. and Liao, C. H. 2020. Mechanism of action of botulinum toxin A in treatment of functional urological disorders. *Toxins*, 12(2), pp. 1–11. DOI: https://doi.org/10.3390/toxins12020129

[66] Osorio, H. M., Castillo-Solís, F., Barragán, S. Y., Rodríguez-Pólit, C. and Gonzalez-Pastor, R. 2024. Graphene Quantum Dots from Natural Carbon Sources for Drug and Gene Delivery in Cancer Treatment. *International Journal of Molecular Sciences*, 25(19). DOI: https://doi.org/10.3390/ijms251910539

[67] Zhang, H. et al. 2013. Uniform ultrasmall graphene oxide nanosheets with low cytotoxicity and high cellular uptake. *ACS Appl. Mater. Interfaces*, 5(5), pp. 1761–1767. DOI: https://doi.org/10.1021/AM303005J/SUPPL_FILE/AM303005J_SI_001.PDF

[68] Matak, I., Bölcskei, K., Bach-Rojecky, L. and Helyes, Z. 2019. Mechanisms of Botulinum Toxin Type A Action on Pain. *Toxins (Basel).*, 11(8), p. 459. DOI: https://doi.org/10.3390/toxins11080459

[69] Wakchaure, M. B. and Menezes, P. L. 2025. Graphene Oxide Aerogels : From Synthesis Pathways to Mechanical Performance and Applications.

[70] Kärki, T. and Tojkander, S. 2021. Trpv protein family—from mechanosensing to cancer invasion. *Biomolecules*, 11(7), pp. 1–23. DOI: https://doi.org/10.3390/biom11071019

[71] Caterina, M. J. and Pang, Z. 2016. TRP channels in skin biology and pathophysiology. *Pharmaceuticals*, 9(4). DOI: https://doi.org/10.3390/ph9040077

[72] Du, J. et al. 2022. A tough fluorescent nanocomposite hydrogel probe based on graphene quantum dots for the selective detection of Fe3+ ions. *Mater. Adv.*, 3(20), pp. 7579–7589. DOI: https://doi.org/10.1039/D2MA00605G

[73] Liu, P. et al. 2025. Elastic properties of force-transmitting linkages determine multistable mechanosensitive behaviour of cell adhesion. *Nat. Phys.*. DOI: https://doi.org/10.1038/s41567-025-02964-z

[74] Dhavalikar, P. et al. 2020. Review of Integrin-Targeting Biomaterials in Tissue Engineering. *Advanced Healthcare Materials*, 9(23). DOI: https://doi.org/10.1002/adhm.202000795

[75] Syama, S. and Mohanan, P. V. 2019. Comprehensive Application of Graphene : Emphasis on Biomedical Concerns. Springer Berlin Heidelberg, 11(1). DOI: https://doi.org/10.1007/s40820-019-0237-5

[76] Sehat-Kashani, S., Naddaf, H. and Hoveizi, E. 2025. Enhancing bone tissue engineering with polyacrylonitrile electrospun scaffolds and graphene quantum dots: A comprehensive approach to regenerative medicine. *BioImpacts*, 15, p. 30835. DOI: https://doi.org/10.34172/bi.30835

[77] Sheets, K., Wunsch, S., Ng, C. and Nain, A. S. 2013. Shape-dependent cell migration and focal adhesion organization on suspended and aligned nanofiber scaffolds. *Acta Biomater*., 9(7), pp. 7169–7177.
DOI: https://doi.org/10.1016/j.actbio.2013.03.042

[78] Bandyopadhyay, A., Mitra, I., Goodman, S. B. and Kumar, M. 2023. Progress in Materials Science Improving biocompatibility for next generation of metallic implants. *Prog. Mater. Sci*., 133, p. 101053.
DOI: https://doi.org/10.1016/j.pmatsci.2022.101053

[79] Li, J., Zeng, H., Zeng, Z., Zeng, Y. and Xie, T. 2021. Promising Graphene-Based Nanomaterials and Their Biomedical Applications and Potential Risks: A Comprehensive Review. *ACS Biomater. Sci. Eng*., 7(12), pp. 5363–5396.
DOI: https://doi.org/10.1021/ACSBIOMATERIALS.1C00875/ASSET/IMAGES/LARGE/AB1C00875_0012.JPEG

[80] Mishra, A., Modi, U., Sharma, R., Bhatia, D. and Solanki, R. 2025. Biomedical Engineering Advances Biochemical and biophysical cues of the extracellular matrix modulates stem cell fate : Progress and prospect in extracellular matrix mimicking biomaterials. *Biomed. Eng. Adv*., 9, p. 100143.
DOI: https://doi.org/10.1016/j.bea.2024.100143